

Simulation of the Solidification and Microstructural Evolution in Steel Casting Processes Using the InterDendritic Solidification Tool

Jyrki Miettinen, Mahesh Somani, Ville-Valtteri Visuri,* Sami Koskenniska, Seppo Louhenkilpi, Timo Fabritius, and Jukka Kömi

InterDendritic Solidification (IDS) is a thermodynamic–kinetic software combined with a microstructure tool developed to simulate the nonequilibrium solidification (non-EQS) of steels. Herein, its main calculation module, solidification (SOL), is introduced, and some essential results of that module, such as the formation of ferrite and austenite in different types of steels during their solidification, and the formation and dissolution of precipitates during subsequent cooling and heating processes, respectively, following solidification, are presented. The non-EQS is compared with equilibrium and poor-kinetics solidification to demonstrate the effect of kinetics on the results using finite solute diffusion and microstructure data. The poor-kinetics solidification is comparable with the modified Scheil simulation ignoring the solid-state diffusion of slowly moving metallic elements. A particular emphasis is made on demonstrating how to use a postprocessing treatment to control the residual ferrite amounts in stainless steels and the extent of precipitation in particular steel. In this context, the phenomena occurring behind the results are discussed. Finally, to validate the simulations of the SOL module, its calculations are compared with numerous solidification measurements, such as the liquidus and solidus temperatures of different steels and the residual ferrite amounts in stainless steels.

1. Introduction


In the past few decades, a good number of mathematical models have been developed to simulate the solidification and microstructure of metallic alloys. Many of these methods have been reviewed by Hu and Argyropoulos^[1] and particularly, those applied in continuous casting, have been reviewed by Thomas.^[2] In continuous casting, it is still difficult to find a comprehensive solidification and microstructure model to be able to track the microstructural evolution along a given industrial process path.^[3] This is due to the use of a very wide range of length scales, along which the important phenomena of solidification and microstructure evolution can occur.

In earlier work, a thermodynamic–kinetic–empirical tool called InterDendritic Solidification (IDS) was developed to simulate the occurrence of interdendritic segregation during the solidification of steels.^[4–7] The model is based on a “gray box” methodology^[5] as it combines both

empirical (black box) and fundamental (white box) models. Recently, significant efforts have been made to decrease the computational expense of the IDS, which has made the tool suitable for online calculations of various parameters during continuous casting.^[8] Its early milestone version^[3] was based on the calculation of thermodynamic equilibrium at the advancing solid/liquid phase interface, depending on the finite kinetics (e.g., by finite solute diffusion in solid) controlled by the solidification process. The tool could be applied for low-alloyed steels including the formation of only some most essential inclusions, like MnS. Thereafter, the tool has been extended to include lots of new features, such as the formation of numerous inclusions and precipitates during solidification and subsequent cooling, formation of eutectic ferrite in stainless steels,^[9] growth of austenite grains,^[10] decomposition of austenite at low temperatures, and calculation of thermophysical material properties. Most of these advancements have been discussed in other studies.^[4,5] The simulations in the current IDS tool are executed using several calculation modules.^[7] The main module is the solidification (SOL) module that describes the solidification process itself and the subsequent ferrite/austenite transformation and

J. Miettinen, V.-V. Visuri, S. Louhenkilpi, T. Fabritius
Process Metallurgy Research Unit
University of Oulu
PO Box 4300, 90014 Oulu, Finland
E-mail: ville-valtteri.visuri@oulu.fi

M. Somani, S. Koskenniska, J. Kömi
Materials and Mechanical Engineering Research Unit
University of Oulu
PO Box 4200, 90014 Oulu, Finland

 The ORCID identification number(s) for the author(s) of this article can be found under <https://doi.org/10.1002/srin.202200120>.

© 2022 The Authors. Steel Research International published by Wiley-VCH GmbH. This is an open access article under the terms of the Creative Commons Attribution-NonCommercial-NoDerivs License, which permits use and distribution in any medium, provided the original work is properly cited, the use is non-commercial and no modifications or adaptations are made.

DOI: 10.1002/srin.202200120

precipitate formation in the solid state, from 1600 °C down to 900 °C (for low-alloy steels) or 600 °C (for high-alloy steels). Below these temperatures, the SOL simulation is continued by calculation of austenite decomposition, conducted using another IDS module, austenite decomposition (ADC).

The present study is focused on providing a detailed assessment of the simulation capabilities of the SOL module. The results of the SOL module calculation are compared with traditional equilibrium solidification (EQS) and poor-kinetics solidification (PKS). These are the two extreme calculation modes applied also in solidification studies, although no attention is paid to the influence of process conditions. Finally, the SOL module calculations are validated with numerous measurements available in the literature.

2. Description of the Solidification Module

SOL module is the main module of the IDS tool applied in the temperature range from 1600 to 900 °C for low-alloyed steels and from 1600 to 600 °C for high-alloyed steels. The steel is regarded as high alloyed containing at least one of the following solute compositions with proportions exceeding as wt%Cr \geq 5, wt%Ni \geq 5, wt%Mn \geq 5, wt%Mo \geq 3, or wt%Si \geq 3. The recommended maximum limits (in wt%) for possible solute and/or impurity components to conduct SOL simulation using the low-alloyed (L) and high-alloyed (H) steels are given as: C = 3.5%(L)–1.5%(H); Mn = 5%(L)–25%(H); Cr = 5%(L)–30%(H);

Mo = 3%(L)–6%(H); Ni = 5%(L)–25%(H); N = 0.1%(L)–0.3%(H); Al, Cu, Si = 3% each, Nb, Ti, V = 0.5% each, P, S = 0.05% both, Ca, Ce, Mg = 0.02% each; and B, O, H = 0.005% each. Note that the maximum composition of 3.5% for carbon is due to the inclusion of high-carbon steels and cast iron to the group of low-alloyed steels. In these high-carbon alloys, somewhat lower composition limits than expressed above are recommended for the other solutes.

2.1. Illustration of Simulation

The calculations of the SOL module are made in one volume element set on the side of a dendrite arm having a hexagonal arm arrangement (see **Figure 1**). In this arrangement, the volume element gets the form of an equilateral triangle, when looking perpendicularly to the dendrite arm growth. This principle has been successfully applied in the earlier modeling work concerning the solidification of steels.^[11] A realistic simulation assumes that 1) the dendritic structure forming in different parts of the strand is quite regular and 2) the solute mixing in liquid is complete, with no solute transport by strong liquid flows causing macrosegregation.

In these calculations, the SOL module applies three thermodynamic models, the conventional substitutional 1) solution model for liquid (L), ferrite (delta ferrite δ and eutectic ferrite ϵ), and austenite (γ), 2) the magnetic ordering model by Hillert and Jarl^[12] for ferrite, and 3) the sublattice model by Sundman and Ågren^[13] for

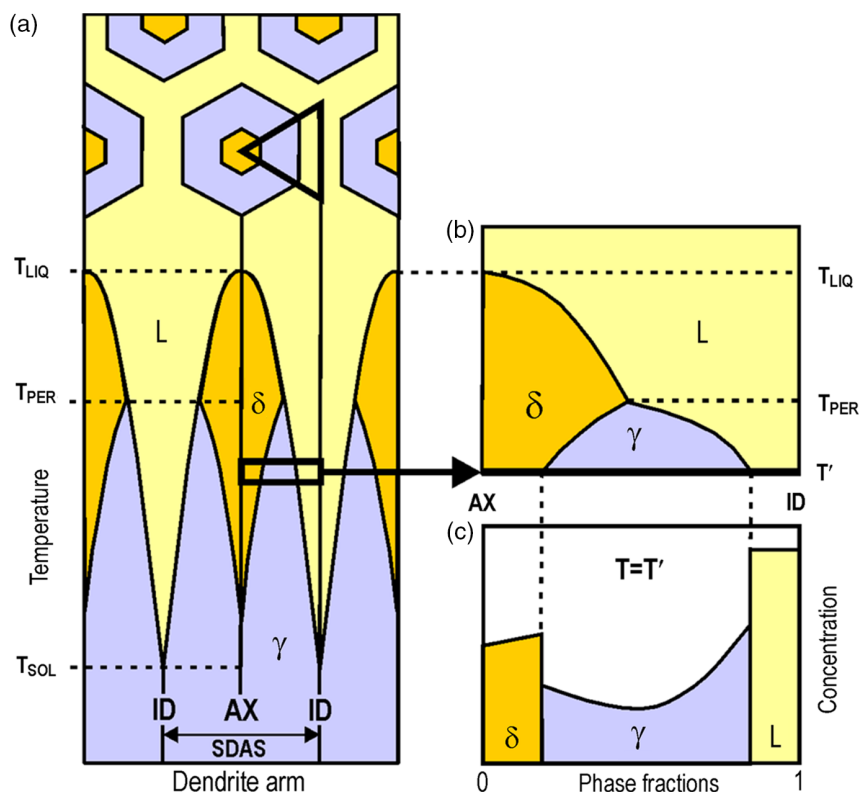


Figure 1. Magnified portion of the mushy zone showing a volume element on the side of a) dendrite arm with b) corresponding phase fractions and c) solute concentration profiles. L = liquid, δ = delta ferrite, γ = austenite, T_{LIQ} = liquidus temperature, T_{PER} = peritectic temperature, T_{SOL} = solidus temperature, AX = dendrite arm axis, ID = interdendritic region, and SDAS = secondary dendrite arm spacing.

the semistoichiometric compounds. The kinetics is taken into account by the solute material balance equations and Fick's diffusion laws.^[4,5] Also included, of course, is time (diffusion time), which comes from the cooling/heating process.

The material data needed in the calculations using the SOL module are taken from the IDS database. It contains the parameters of Gibbs energy data, solute diffusion coefficients, and microstructure (dendrite arm spacing and grain size) concerning the elements Fe, C, Si, Mn, P, S, Cr, Mo, Ni, Cu, Al, N, Nb, Ti, V, Ca, Ce, Mg, B, O, and H. All these data have been adequately validated with many experimental measurements. A significant part of this database is the Gibbs energy data of the solution phases (liquid, ferrite, and austenite) and different compounds (such as sulfides, oxides, carbides, nitrides, and borides). These data are taken from the Iron Alloy Database (IAD), developed to give consistent and simple-format thermodynamic data for the IDS tool. The first three parts of this databank have recently been published.^[14–16] The other essential input data are the solute diffusion coefficients for ferrite and austenite and the parameters for the calculation of the secondary-dendrite arm spacing (SDAS). By controlling the kinetics of solidification, these parameters provide the necessary background for the simulation of non-EQS.

Depending on the composition, the steel undergoing solidification goes through one of the following paths before the onset of austenite decomposition process: A) $L \rightarrow L + \delta \rightarrow \delta + \gamma + \delta (\rightarrow \gamma)$, B) $L \rightarrow L + \delta \rightarrow L + \gamma + \delta \rightarrow \gamma + \delta (\rightarrow \gamma)$, C) $L \rightarrow L + \gamma \rightarrow \gamma$, i.e., after the list of paths for the austenite decomposition process. Here, the notations L, δ , and γ denote liquid, delta ferrite, and austenite phases, respectively.

The mutual order of the phases in the above paths (A) through (C) shows how the phases are located in the volume element of Figure 1, that is, from the dendrite arm axis (left) to the interdendritic region (right). In the two-phase regions of $L + \delta$, $L + \gamma$, and $\gamma + \delta$, transformations of $L \rightarrow \delta$, $L \rightarrow \gamma$, and $\delta \rightarrow \gamma$ take place, respectively, and in the three-phase region of $L + \gamma + \delta$, a peritectic transformation of $L + \delta \rightarrow \gamma$ takes place. In the former case, the moving-phase interfaces are δ/L , γ/L , and γ/δ , respectively, and in the latter case, both the γ/L and the γ/δ phase interfaces are present, the former (γ/L) moving toward the interdendritic area and the latter (γ/δ) moving toward the dendrite axis. Note that the solid structure before the start of the austenite decomposition process may contain both austenite and ferrite

and not necessarily only the austenite (see paths A and B). In addition, the eutectic ferrite, ϵ , may form from the liquid phase near the γ/L phase interface. This may occur in the final stage of austenitic solidification of stainless steels, when ferrite-stabilizing solutes, such as Cr and Mo, start to enrich the γ/L phase interface. This results in an additional transformation of $L \rightarrow \gamma + \epsilon$ along the paths B and C. During that transformation, two-phase interfaces, γ/L and ϵ/L , move simultaneously toward the interdendritic area, instead of one γ/L interface. In this case, we have simplified the mathematical treatment by simulating the movement of the γ/ϵ phase interface perpendicular to the movement of the γ/L phase interface, toward the γ side of the γ/L interface. This simplified treatment was adopted from Koseki et al.^[9] to avoid the complex mathematical treatment related to the eutectic growth in a pure γ region as well as the possible γ/δ phase interface behind it. Also, the disappearance of eutectic ferrite below the solidus can then be easily simulated, in the form of $\epsilon \rightarrow \gamma$ transformation perpendicular to the growth of the original γ/L phase interface. Due to the small amounts of eutectic ferrite formed in stainless steels, the above approximations can be considered reasonable. As a result of all these calculations, one gets the fractions and the compositions of each phase as a function of the decreasing temperature.

Figure 2 shows the SOL module flow chart and its phase blocks, where the calculations are conducted. In a continuous cooling case, all phase block simulations are conducted for a decreasing temperature profile. In the mushy zone phase blocks, the temperature must decrease continuously, even if extremely slowly, but in the solid-state phase blocks (below the solidus), the temperature can increase, too. In this respect, the simulation suits well for the determination of residual ferrite amount in stainless steels, as well as the formation or dissolution of precipitates in any steel depending on the applied postsolidification heat treatment. These properties can also be calculated in continuous casting strands, whose surface temperatures may occasionally increase, though this implies, of course, the coupling of IDS with a heat transfer model of the continuous casting process.^[8] In addition, due to the possible increase in temperature, we may have to get back to certain phase blocks left earlier. A bidirectional module change is possible for the phase blocks connected by the thick double arrows. In most continuous casting cases, the “two-way visits” shown in Figure 2 are adequate.

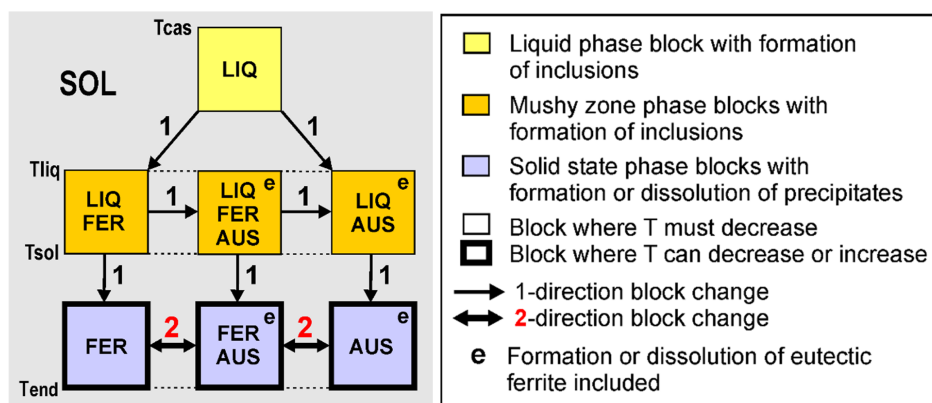


Figure 2. SOL module flow chart and phase blocks.

Detailed descriptions of the calculation strategy and the corresponding equations (e.g., for the moving δ/L , γ/L , and δ/γ phase interfaces) have been given in the earlier papers.^[4,5] In this context, we present the equations only for the precipitation of one binary compound, NbC, from austenite. These equations are applied in the phase blocks FER + AUS and AUS in Figure 2.

2.2. Equations for Simulating NbC Precipitation from Austenite

The precipitation of NbC (θ) from austenite is simulated with the following set of equations

$$G_{\text{NbC}}^* + \Delta G_{\text{NbC}}^I + \Delta G_{\text{NbC}}^M = \mu_{\text{Nb}}^{\gamma}(T, x_1^{\gamma}, \dots, x_n^{\gamma}) + \mu_{\text{C}}^{\gamma}(T, x_1^{\gamma}, \dots, x_n^{\gamma}) \quad (1)$$

$$\Delta f^{\theta}(x_{\text{Nb}}^{\theta 0} - x_{\text{Nb}}^{\gamma}) = f^{\theta}(x_{\text{Nb}}^{\theta} - x_{\text{Nb}}^{\theta 0}) - S_{\text{Nb}}^{\gamma/\theta}(x_{\text{Nb}}^{\gamma}, D_{\text{Nb}}^{\gamma}) \quad (2)$$

$$\Delta f^{\theta}(x_{\text{C}}^{\theta 0} - x_{\text{C}}^{\gamma}) = f^{\theta}(x_{\text{C}}^{\theta} - x_{\text{C}}^{\theta 0}) - S_{\text{C}}^{\gamma/\theta}(x_{\text{C}}^{\gamma}, D_{\text{C}}^{\gamma}) \quad (3)$$

where G_{NbC}^* is the Gibbs energy (J mol⁻¹) of formation of NbC from pure α -Nb and graphite-C, ΔG_{NbC}^I and ΔG_{NbC}^M are the barrier energies (J mol⁻¹) of incubation and volume misfit,^[6] μ_{Nb}^{γ} and μ_{C}^{γ} are the chemical potentials (J mol⁻¹) of Nb and C in austenite (γ) related to the pure α -Nb and graphite-C, respectively, T is the temperature (K), x_{Nb}^{γ} and x_{C}^{γ} are the γ/θ interface compositions (mole fraction) of Nb and C in austenite, n is the number of components in the alloy (with $i = 1$ for Fe), f^{θ} is the NbC fraction, Δf^{θ} is the fractional movement of the γ/θ interface, and $x_{\text{Nb}}^{\theta 0}$ and $x_{\text{C}}^{\theta 0}$ are the Nb and C compositions in NbC before movement Δf^{θ} . The term $S_{\text{Nb}}^{\gamma/\theta}$ includes Fick's first law of diffusion and describes the amount of Nb and C in austenite leaving the γ/θ interface. Its general form in this presentation is $S_{\text{Nb}}^{\gamma/\theta} = -4D_{\text{Nb}}^{\gamma}\Delta t C_{\text{Nb}}^{\gamma/\theta} \text{SDAS}^{-2}$, where D_{Nb}^{γ} is the diffusion coefficient (cm²s⁻¹) of solute Nb or C in austenite, Δt is the time (s) spent during the fractional movement of the γ/θ interface, $C_{\text{Nb}}^{\gamma/\theta}$ is the dimensionless concentration gradient at the γ/θ interface obtained by solving Fick's second law of solute diffusion in austenite,^[4,5] and SDAS is the secondary dendrite arm spacing (cm). Time increment Δt is related to the temperature T as $\Delta t = \Delta T/\text{CRT}$, where ΔT is the temperature step of calculations (K) and CRT is the cooling or the heating rate (°C s⁻¹) of the process. The calculations with Equation (1) through (3) are made stepwise by decreasing or increasing the temperature as $T = T + \Delta T$, depending on whether we have a cooling or heating process. At each temperature, the austenitic interface compositions, x_{Nb}^{γ} and x_{C}^{γ} , and the fractional movement of the interface, Δf^{θ} , are solved from these three equations. Note that at a fixed temperature, terms $S_{\text{Nb}}^{\gamma/\theta}$ are constant and terms μ_{Nb}^{γ} and μ_{C}^{γ} are the functions of the interface composition, comprising all the components including iron.

The barrier energy of incubation delays the formation of a precipitate, and the volume misfit energy restrains its growth as described by the simple phenomenological equations available in the study by Miettinen.^[6] Neither of these energies was earlier included in the calculations. **Figure 3** shows schematically how the inclusion of these new energies stated above changes the total

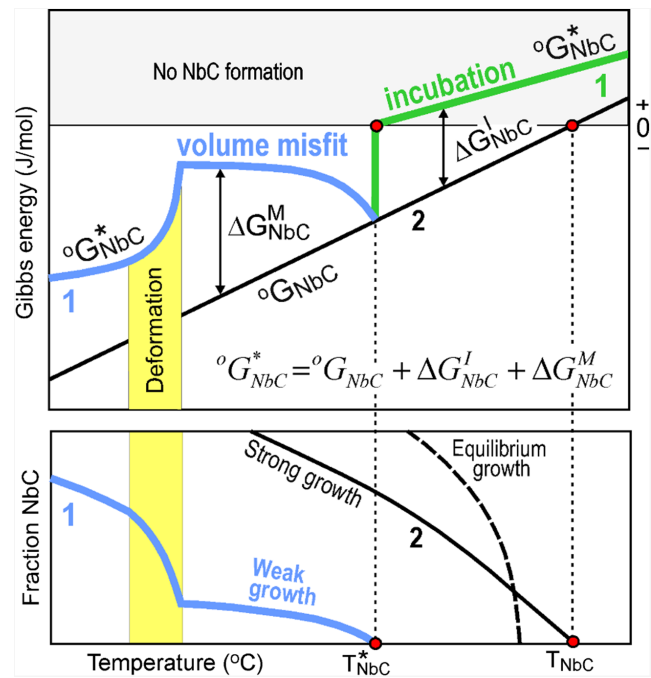


Figure 3. Schematic presentation of Gibbs energy of formation of NbC (upper figure) and the fraction of NbC formed (lower figure) as a function of temperature, when 1) including the barrier energies and when 2) excluding them.

Gibbs energy expression: $G_{\text{NbC}}^{*} = G_{\text{NbC}}^* + \Delta G_{\text{NbC}}^I + \Delta G_{\text{NbC}}^M$ for NbC, that is, the left-hand side of Equation (1). The first term ΔG_{NbC}^I increases with decreasing temperature due to the decreasing solute diffusion in austenite. The higher the cooling rate, the stronger this increase. At temperature T_{NbC}^* , we finally get a negative value for G_{NbC}^{*} and hence, the formation of NbC can start. From that moment onward, the term ΔG_{NbC}^I starts to decrease. This increases the driving force of NbC enabling its formation from the undercooled state. At the same time, however, the term ΔG_{NbC}^M starts to increase effectively. This is related to the high density of still finer particles, whose growth is effectively restrained. As their sizes increase, the total precipitate-matrix surface decreases as a result of decreasing number of the particles. This ceases the growth of the volume misfit, as shown in the figure. Due to deformation, we can get a sudden drop of volume misfit. This can be explained in respect of the increased formation of dislocations. However, with ceasing deformation at lower temperatures, volume misfit starts to increase once again. As shown in Figure 3, due to the positive values of terms ΔG_{NbC}^I and ΔG_{NbC}^M , NbC starts to form at a lower temperature and its growth becomes weaker (curve 1) in comparison with the case where the terms are not included (curve 2). Even stronger is the growth simulated with thermodynamic software, which does not account for the kinetics (broken line). In this case, the precipitation is likely to start at a temperature lower than the temperature for the start of NbC formation (T_{NbC}), due to the lower interdendritic Nb composition obtained by EQS.

2.3. Input and Output Data

For the user, the input data of the SOL module simulations is very simple. The two essential input parameters are the nominal composition of the steel and the cooling rate of solidification. The cooling rate can be a constant value or a process data table, including columns of time, temperature, and deformation. The latter alternative allows to make successive cooling and heating treatments for the steel, as well as to study the effect of deformation on the results. For the present calculations, the deformation has been linked to accelerate the solute diffusion around the precipitates and reduce the precipitation barriers (incubation and solute misfit) that accelerate the precipitation. The calibration of the degree of deformation leading to a proven enhancement of precipitation, however, is still in progress. The process data file, if produced by an online heat transfer model of continuous casting, gives an excellent possibility to simulate the steel solidification in the selected strand intersections. However, the file can also be produced by the user, to test the effect of actual cooling, heating, and deformation on the results. It is worth noting that due to the finite kinetics, the SOL simulation is not reversible, but its results are affected by all possible cooling and heating treatments.

The third input parameter of the simulation is the SDAS. A value for this parameter can be given by the user or its value can be calculated by the SOL module, depending on the applied cooling rate. By fixing the diffusion distances in the volume element, parameter SDAS has a clear effect on the progress of solidification. Its value is also used as the initial value for the size of austenite grains, whose growth is calculated below the solidus.

Using the above-mentioned input data (and the Gibbs energy, diffusion, and microstructure data of the IDS database), the SOL module simulates or calculates: 1) solidification of steel (ferritic, austenitic, and peritectic solidification); 2) enrichment or impoverishment of solutes in liquid; 3) formation of various compounds (inclusions) from liquid; 4) homogenization of solute microsegregation below the solidus; 5) the ferrite–austenite transformation taking place below the solidus; 6) formation and dissolution of eutectic ferrite (in high-alloyed steels only); 7) formation and dissolution of various compounds (precipitates) in the solid structure; and 8) growth of austenite grains.

These results are shown in a compact form in three IDS output files as a function of temperature. The first file is the phase fraction file showing the fractions of liquid, primary ferrite (δ), austenite (γ), eutectic ferrite, and compounds (total fraction). These results for ferrite, austenite, and liquid are illustrated in Figure 1b. The second file is a compound fraction file showing the fractions of the individual compounds (inclusions or precipitates). The possible compounds of simulation are AlN, BN, CrN, Cr₂N, Si₃N₄, TiB₂, CaS, MgS, H₂(g), N₂(g), FeMo₂B₂, Fe₃Mo₃C, FeNbB, Ti₂CS, (Mn,Fe)S, (C,N)Nb, (C,N)Ti, (C,N)V, (Cr,Fe)₂B, (Fe,X)₂B (X = Cr,Mn,Ni,V), (Cr,Fe)₂₃C₆, (Cr,Fe)₇C₃, (BC)₆Fe₂₃, (Fe,X)₃C (X = Cr,Mn,Mo), (Cr,Ni)₈Fe₉ (\approx sigma), together with several simple oxides, such as Al₂O₃, B₂O₃, CaO, Ce₂O₃, Cr₂O₃, Fe_{0.947}O, MgO, MnO, SiO₂, and Ti₂O₃. The third file type is the concentration profile file showing the global, dendrite axis, and interdendritic compositions for all solutes, as well as their compositions in delta ferrite, austenite, eutectic ferrite, and

liquid. These results, for ferrite, austenite, and liquid, are illustrated in Figure 1c. The concentration profile file is the most extensive of these files containing 37 phase composition values at each temperature. In addition, files contain notations for the important events of solidification, such as 1) start of solidification (i.e., the liquidus temperature), 2) start of local strengthening (75% of the local structure solidified), 3) end of solidification (i.e., the solidus temperature), 4) start of primary ferrite formation, 5) disappearance of primary ferrite (i.e., the end of the peritectic transformation, if the liquid is present), 6) start of austenite formation (i.e., the start of peritectic transformation if liquid and ferrite are present), 7) disappearance of austenite, 8) start of eutectic ferrite formation (only for high-alloyed steels), 8) disappearance of eutectic ferrite (only for high-alloyed steels), 9) start of compound formation (for inclusions and precipitates), and 10) disappearance of compound (for precipitates only, below the solidus).

3. Calculations Using the SOL Module

This section shows some essential results obtained by the SOL module of the IDS tool. The nominal compositions of the investigated steels are given in Table 1. First, SOL-based calculations of solidification, solute enrichment, and precipitation are compared with those of equilibrium (lever rule) solidification and PKS. The latter calculations are comparable with those of the Scheil solidification model,^[17] further modified by Chen and Sundman^[18] to get reasonable results without making time-consuming calculations of kinetics using the thermodynamic software, such as Thermo-Calc.^[19] By that modification, the fast-diffusing interstitial solutes, such as C, N, and B, are treated as lever-rule components. Next, SOL calculations are shown to demonstrate the effect of alloying on steels solidification and the residual ferrite amount in stainless steels. The point worth emphasizing is the sluggish disappearance of residual ferrite in comparison with equilibrium calculations. Third, the example calculations are presented to show the effect of postsolidification heat treatment on the residual ferrite amount in stainless steel and on the formation and dissolution of precipitates NbC and

Table 1. Nominal compositions of the five steels grades studied (A, 205, 404, 413, and B).

| Solute [wt%] | Steel grade | | | | |
|--------------|-------------|-------|-------|-------|-------|
| | A | 205 | 404 | 413 | B |
| C | 0.15 | 0.36 | 0.036 | 0.013 | 0.05 |
| Si | 0.50 | 0.27 | 0.44 | 0.48 | 0.50 |
| Mn | 1.00 | 0.58 | 1.25 | 1.74 | 1.50 |
| P | – | 0.015 | 0.025 | – | 0.02 |
| S | – | 0.012 | – | 0.003 | 0.02 |
| Cr | – | 0.08 | 18.40 | 19.20 | 18.00 |
| Mo | – | 0.02 | 0.38 | 4.44 | 0.50 |
| Ni | – | 0.05 | 9.10 | 25.40 | 8.00 |
| Cu | – | – | 0.20 | 1.51 | – |
| Nb | 0.03 | – | – | – | – |
| N | – | – | 0.081 | 0.035 | 0.05 |

Nb(C,N) in low-alloyed steels. By such simulations, the user may chart the possibilities to control the ferrite and precipitate amounts in his steel, both affecting the properties of that steel.

3.1. Comparison of SOL Calculations with those of EQS and PKS Modes

The EQS mode, EQS (or lever rule), assumes infinitely fast diffusion for all solutes, not only in the liquid phase but also in the solid state. It is widely applied in thermodynamic software while paying no attention to the kinetics of solidification. Consequently, these calculations give too high solidus for the considered alloys and overestimate the amounts of precipitates formed, in contrast to the measurements made by finite cooling rates. Another way to “avoid” the inclusion of kinetic calculations in a solidification model is to ignore the solute diffusion in solid, as suggested by Scheil.^[17] In that case, however, the solidification can be terminated simply by a eutectic reaction (if typical for the alloy), which finally stops the strong temperature drop at the end of solidification. To prevent such solidus drops, Chen and Sundman^[18] modified the Scheil model by assuming extremely rapid solid-state diffusion for the fast-diffusing interstitial solutes, such as C, N, and B. Consequently, the solidus is raised to a more realistic value, between the equilibrium solidus and that predicted by the Scheil treatment. By coupling the method by Chen and Sundman^[18] to the thermodynamic software, the latter can be used to give a somewhat better estimation of the real solidification process, without including the complex and time-consuming calculations of kinetics in the simulation. It is noteworthy that also available are the analytical solute redistribution equations, which approximately simulate the solute back diffusion in solid.^[20] Neither can these equations be combined reliably with thermodynamic calculations of multicomponent alloys, nor do they give any information about the solute concentration profiles formed after solidification.

In the SOL module, the kinetic calculations are also included, by taking into account the finite solute diffusion in ferrite and austenite. In this way, the SOL module has similarities with the sophisticated thermodynamic-kinetic software DICTRA,^[21] although the focus of the SOL has been only on the rapid simulation of steels solidification and the accompanying phase transformations. The SOL module can also be used to simulate the EQS and the PKS. The latter simulation is comparable with that of the modified Scheil solidification,^[18] except that the PKS treatment still allows extremely slow diffusivities for the substitutional components, to avoid failure of calculations in SOL. In addition, the PKS treatment is applied also below the solidus temperature for the advancing δ/γ phase interface and the formation of precipitates, whereas the modified Scheil treatment is typically applied for the solidification event only.

Figure 4 shows the calculated phase fractions for the solidified low-alloyed steel A. As shown, the solidus determined by the SOL calculations is lower than that obtained by the EQS calculations but higher than that obtained by the PKS calculations. This is because of the finite (and experimentally validated) solute diffusivities applied in SOL. The solidus drop predicted by PKS calculations can be considered quite steep considering

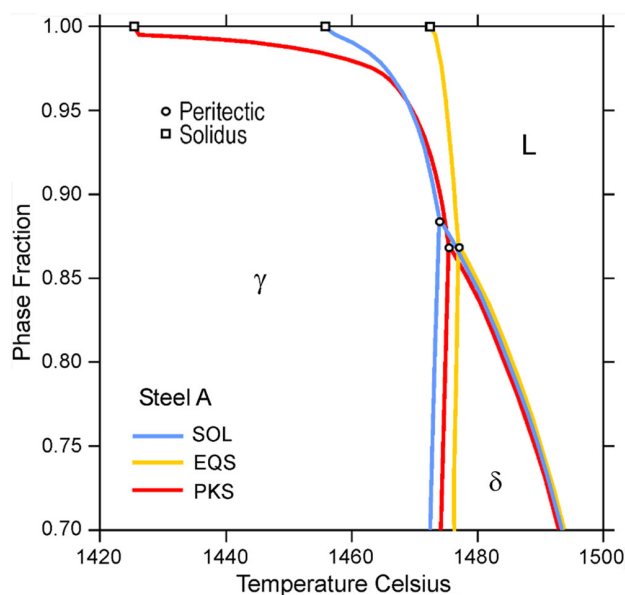


Figure 4. Calculated phase fractions of steel A (Table 1) as a function of temperature. The cooling rate of SOL calculations was 1°C s^{-1} .

the low solute amounts of steel A. A larger drop was prevented only by the earlier fixed decision to terminate all solidification calculations of SOL with a liquid fraction of 0.005, corresponding to the solidus temperature of the steel. This is a practical choice made to avoid failing calculations at the end of solidification.

Figure 5 shows the calculated interdendritic compositions of Mn and Nb in steel A. Again, the SOL-calculated results are located between those of EQS and PKS calculations. Particularly noteworthy is the gradual homogenization of the SOL-calculated interdendritic compositions in austenite below the solidus after the disappearance of the liquid phase, whereas those by the EQS calculations become directly identical to their nominal compositions. By the PKS calculations, the interdendritic Mn composition remains very high, as it must adopt the composition of the last liquid drop at the solidus, due to the ignorable back diffusion in austenite. As no compounds of Mn, such as MnS, are formed, this strong concentration peak then remains in the interdendritic region of austenite. In the case of Nb, the trend is similar to that of Mn except that just below the solidus, NbC is formed. With decreasing temperature, the formation of NbC is enhanced by the increasing driving force for its formation. The NbC growth is supported by the continuous feeding of the rapidly diffusing carbon from the environments of the interdendritic region. This consumes the interdendritic concentration peak of Nb quite rapidly because, in the PKS calculations, no excess Nb can diffuse from the environments. Below 1420°C , carbon has been consumed so much that the NbC formation starts to cease. Consequently, the interdendritic Nb composition does not anymore decrease so effectively.

Figure 6 shows the calculated amounts of NbC in steel A. Note the much weaker formation of NbC is predicted by the SOL calculations compared with the EQS calculations. The weaker formation of NbC as predicted by the SOL calculations is due

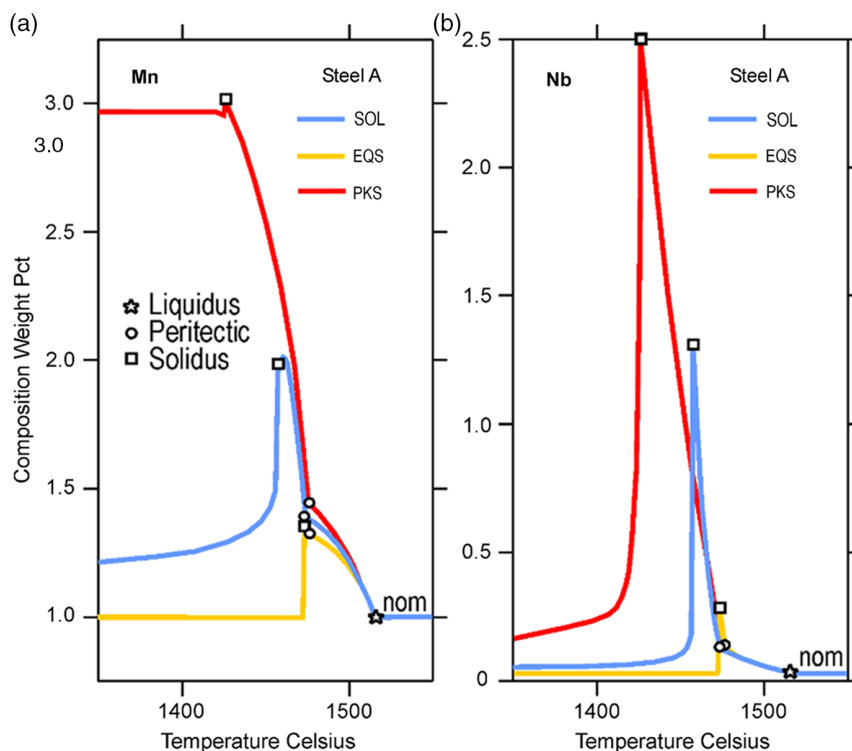


Figure 5. Calculated interdendritic compositions of a) Mn and b) Nb in steel A (Table 1) as a function of temperature. The cooling rate of SOL calculations was 1°C s^{-1} .

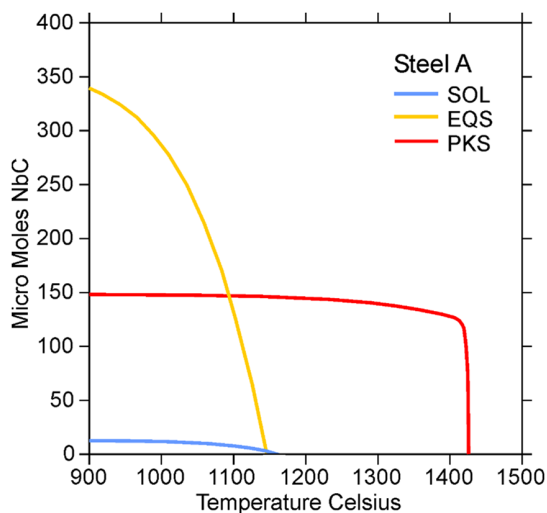


Figure 6. Calculated amounts of NbC in steel A (Table 1) as a function of temperature. The cooling rate of SOL calculations was 1°C s^{-1} .

to the precipitation barriers and the poor solute diffusion at such low temperatures, whereas in EQS calculations, we have no precipitation barriers and infinitely rapid solute diffusion. Consequently, the EQS-based start temperature of NbC formation could be expected to be higher than that calculated by SOL, but the latter temperature is still a bit higher. This is due to the inclusion of microsegregation of Nb in the SOL

calculations, which keep the interdendritic Nb composition much higher than that in the EQS calculations (see Figure 5). As for the PKS calculations, NbC starts to form at a very high temperature, just below the solidus, as explained in the context of Figure 5. The growth of NbC below that temperature is very fast, owing to the very high interdendritic Nb composition. However, due to the rapid consumption of carbon in NbC, the growth of NbC finally ceases. According to Figure 6, this happens below 1420°C , which agrees well with the slowing down of the depletion of interdendritic Nb composition in Figure 5.

3.2. Effect of Alloying on Solidification and Ferrite Content

Alloying is the most dominating factor affecting the solidification of steels. **Figure 7** shows the calculated phase fractions in the solidified steels 205, 404, and 413 using the three methods. The high-alloyed stainless steel 413 is shown to solidify at a temperature about 60°C lower than the less-alloyed stainless steel 404 and about 100°C lower than the low-alloyed carbon steel 205. The calculated liquidus and solidus temperatures of all three steels agree well with the values reported by Jernkontoret.^[22] The solidification of steel 413 leads purely to austenite formation, while steels 205 and 404 solidify through a peritectic transformation, starting at 1485 and 1435°C , respectively. Also, these temperatures agree fairly well with the measured values,^[22] that is, 1483 and 1424°C . For stainless steels 404 and 413, also shown are the phase fractions calculated with the EQS mode and the PKS mode. As expected from the results of Figure 4, the EQS

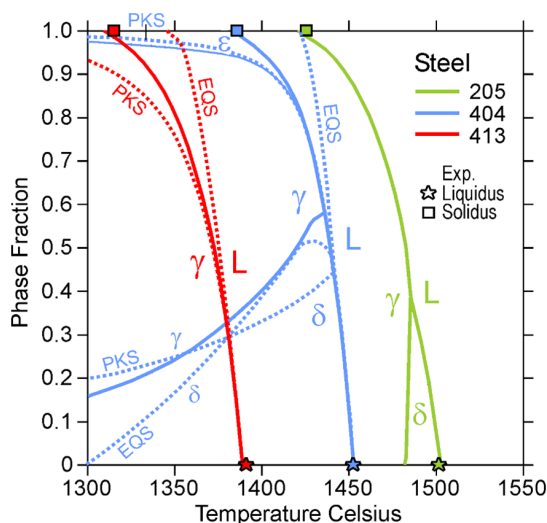


Figure 7. Calculated phase fractions of steels 205, 404, and 413 (Table 1) as a function of temperature, together with experimental liquidus and solidus temperatures.^[22] The cooling rate in SOL calculations and measurements was $0.5\text{ }^{\circ}\text{C s}^{-1}$.

calculation keeps the solidus too high and the PKS calculation makes it drop too low. In the case of stainless steels, however, the solidus temperatures have now dropped as low as $1165\text{ }^{\circ}\text{C}$ (steel 404) and $1100\text{ }^{\circ}\text{C}$ (steel 413). These are certainly not the acceptable input parameters for heat transfer models, which simulate the solidification of a macroscopic process, such as continuous casting. In addition, the residual ferrite amount in steel 404 becomes quite different by the EQS and PKS calculations. In the former case, ferrite disappears already at $1300\text{ }^{\circ}\text{C}$, and in the latter case, more ferrite is retained in the solid structure than obtained by SOL. This happens despite the late start of austenite formation in the calculations of SOL. Also, worth noting is the eutectic ferrite (ϵ) formed in the final stages of the solidification of steel 404. By offering faster diffusion rates for the solutes, it restrains the solute enrichment in liquid (caused by the presence of austenite), thereby raising the solidus temperature slightly. Furthermore, the PKS mode would allow the formation of eutectic ferrite, above the solidus, but that was neglected to clarify the presentation in the figure. The EQS mode, instead, simulates the formation of only one ferrite, without dividing it into the delta and eutectic ferrites.

Another way to demonstrate the effect of alloying on solidification is to construct a dynamic phase diagram for the steel. Such a diagram is presented in **Figure 8**, showing the effect of Ni composition on the high-temperature phase regions of steel B. Note the light-yellow region showing the presence of eutectic ferrite. This phase is formed during austenitic solidification due to the enrichment of Cr and Mo in liquid. With small amounts, at the advancing γ/L phase interface, these can prevent solidification cracking in austenitic stainless steels.^[23,24] Also note the effect of increasing Ni composition in dropping the temperature, where eutectic ferrite starts to form. This is, of course, due to the increasing austenite stability, though some sudden drops may also be as a result of stepwise calculations in SOL. The calculations using SOL were also compared with those of EQS using the

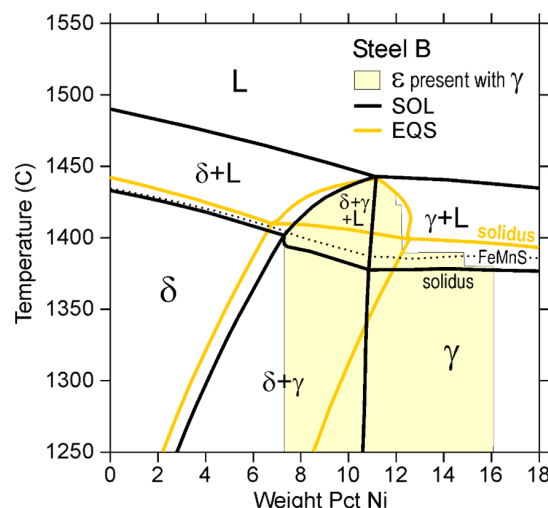


Figure 8. Calculated phase regions of steel B (Table 1) as a function of nickel composition. The cooling rate in SOL calculations was $1\text{ }^{\circ}\text{C s}^{-1}$. FeMnS = formation of (Fe,Mn)S.

Thermo-Calc software. These results show somewhat higher solidus and somewhat narrowed ferritic and peritectic regions in **Figure 8**. At about $1420\text{ }^{\circ}\text{C}$, the peritectic region extends up to 12.6 wt\% Ni by EQS calculations but only up to 11 wt\% Ni by SOL calculations. This difference, however, is compensated by the SOL-calculated eutectic ferrite. At $1250\text{ }^{\circ}\text{C}$, noteworthy is the presence of SOL-calculated eutectic ferrite up to 16 wt\% Ni , whereas the slope of the δ/γ boundary by EQS calculations indicates the rapid disappearance of ferrite at lower temperatures.

Figure 9 introduces another type of dynamic diagram for steel B. Here, we see how the Ni composition affects the amounts of delta and eutectic ferrites at the solidus and $700\text{ }^{\circ}\text{C}$. At $700\text{ }^{\circ}\text{C}$, the

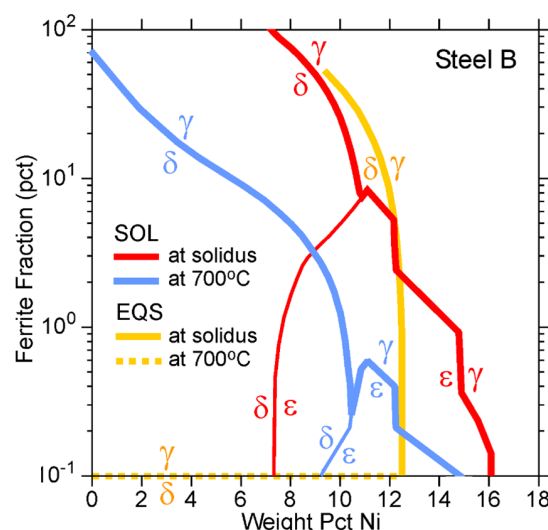


Figure 9. Calculated delta and eutectic ferrite amounts of steel B (Table 1) at solidus and $700\text{ }^{\circ}\text{C}$ as a function of nickel composition. The cooling rate in SOL calculations was $1\text{ }^{\circ}\text{C s}^{-1}$.

amounts of both ferrite types have decreased considerably from the values at the solidus, as shown by the red and blue curves. Note some sudden drops in these curves, which correspond to the temperature drops in Figure 8, at the same Ni compositions. According to EQS calculations, conducted using the ThermoCalc software, no eutectic ferrite forms at the solidus, but the amount of delta ferrite formed agrees reasonably well with the total ferrite amount of SOL calculations, up to 12.2 wt% Ni. At 700 °C, however, there is no delta ferrite left according to the EQS calculations, for any given Ni composition. This example clearly shows the important role of kinetics and the process conditions in trying to control the amount of residual ferrite forming in the steel. More detailed discussions of this feature are given in the next section, describing the effect of post-treatment on the ferrite control.

3.3. Effect of Postsolidification Heat Treatment on Ferrite Content

In the previous section, some example calculations were shown to demonstrate the effect of alloying on the residual ferrite content of stainless steels. The amount of ferrite is known to affect the steel properties,^[25] for example, with respect to solidification cracking and hot formability.^[23,24,26] As a strong barrier to the dislocation motion, ferrite can restrain grain growth, increase strength, and reduce fatigue properties.^[27] It can also lead to detrimental effects on the high-temperature workability and corrosion resistance^[28,29] and cause an unfavorable magnetic

character to the material.^[30] Alloying, however, cannot always be used to control the ferrite content of the structure. Another way is to use post-treatment processes.^[25,31,32] In the following, post-solidification heat-treatment calculations conducted using the SOL module are shown to demonstrate the effect of process conditions (time and temperature) on the residual ferrite contents in stainless steels. No experimental measurements are available for these example calculations, but a general validation for the calculated and measured ferrite amounts in stainless steels is presented in Section 4.7.

Figure 10 shows the calculated residual ferrite amounts in steel B solidified at the linear rates of 1 and 10 °C s⁻¹, heated at a rate of 5 °C s⁻¹, held for 60 min at 1100 °C (red curves) and 1200 °C (blue curves), and then cooled at a rate of 1 °C s⁻¹. In all cases, ferrite tends to stay in the structure, whereas according to EQS calculations, it already disappears at 1228 °C. With the higher rate of solidification, the as-cast ferrite fraction at 700 °C would be slightly higher (5.6 pct) than that achieved via the lower rate (5.3 pct). This is due to the shorter time available for solute diffusion at the higher cooling rate (10 °C s⁻¹), although the smaller SDAS value (27 μm) offering shorter diffusion distances for the solutes has prevented the ferrite amount from getting even larger. Consequently, during post-treatment indicated by the red and the blue curves, the ferrite amounts start to decrease, as the as-cast solute microsegregations are homogenized. Due to the improved kinetics at 1200 °C, of course, the rate of ferrite dissolution is higher than that at 1100 °C. Even more interesting is the fact that in the finer

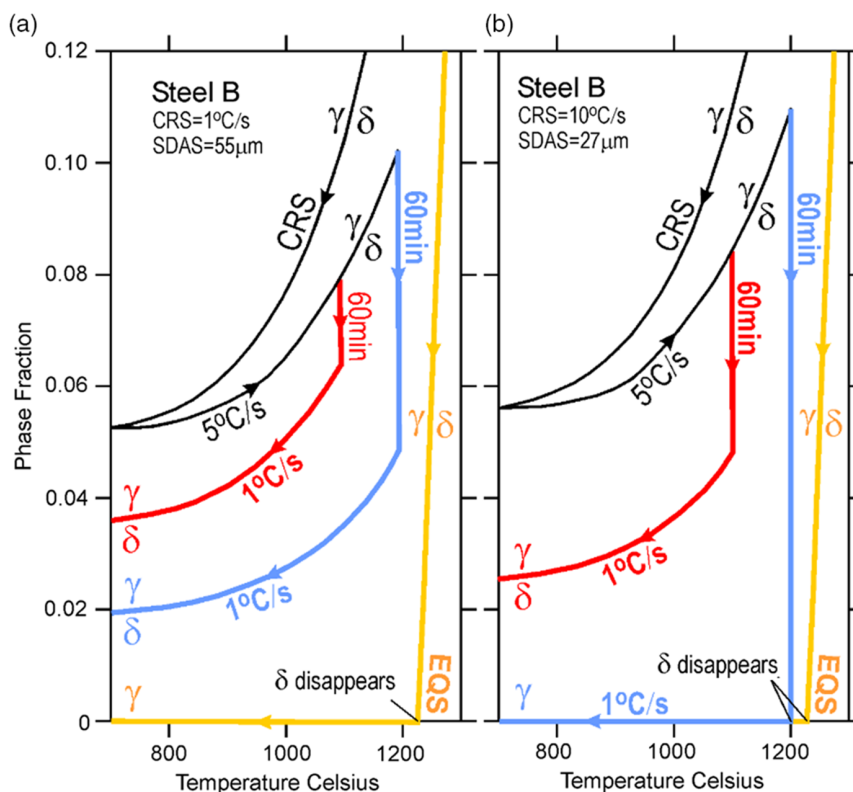


Figure 10. Calculated residual ferrite amounts in steel B (Table 1) solidified with rates of a) CRS = 1 °C s⁻¹ and b) CRS = 10 °C s⁻¹, heated with a rate of 5 °C s⁻¹, and held and cooled as shown by the data of the red and blue curves.

dendritic structure ($SDAS = 27 \mu m$), the ferrite dissolution is enhanced, such that it completely disappears at $1200^\circ C$. This is not unexpected, as the solute concentrations are now close to those of EQS.

The previous example showed the effect of the limited solute diffusion (or time) to cease the ferrite dissolution in stainless steels. Due to the low Cr and Mo diffusivities in austenite, their compositions in the ferrite side of the moving / phase interface may become very high, promoting the formation of brittle phases, such as $M_{23}C_6$ carbide and sigma phase, in ferrite. **Figure 11** shows the calculated concentration profiles of Cr and Ni in steel B, solidified at the rates of 1 and $10^\circ C s^{-1}$. The results are measured at $1000^\circ C$ following solidification and after the post-treatment case of 60 min at $1200^\circ C$ of Figure 10. Worth noting are the results concerning the strong enrichment of Cr and the strong depletion of Ni in ferrite at both cooling rates. Otherwise, the cooling rate has only a minor effect on the results of as-cast steel B. After post-treatment, the Cr enrichment and Ni depletion in the coarser structure ($SDAS = 55 \mu m$) become even stronger, as the amount of ferrite decreases. In the finer structure ($SDAS = 27 \mu m$), however, ferrite is completely dissolved, and the dendrite arm axis inherits the austenitic solute compositions. The composition profiles are now well homogenized (quite close to those of EQS calculations), which can be expected to improve the steel quality.

Nevertheless, there is still remarkable precipitation at the ferrite side of / phase interface, as the steel is cooled further, below

$1000^\circ C$. With the lower solidification rate ($1^\circ C s^{-1}$), $M_{23}C_6$ and sigma phases formed at 844 and $744^\circ C$, respectively (following solidification), and these phases disappeared at 889 and $879^\circ C$, respectively (during heating). During final cooling, $M_{23}C_6$ formed once again at $865^\circ C$, such that its final amount at $600^\circ C$ was 47 mol, but the sigma phase did no longer precipitate. With the higher solidification rate ($10^\circ C s^{-1}$), $M_{23}C_6$ and sigma phases did form at 710 and $760^\circ C$, respectively (after solidification), but they disappeared at 855 and $890^\circ C$, respectively (during heating). During final cooling, neither $M_{23}C_6$ nor sigma phase formed, presumably due to the disappearance of the ferrite phase during holding at $1200^\circ C$. Consequently, the risk for cracking is reduced. Note that $M_{23}C_6$ carbide did form also in the interdendritic region during first cooling after solidification, but after the post-treatment process and the following cooling, there was no $M_{23}C_6$ left in the structure.

3.4. Effect of Post-Treatment on Precipitation

In casting and tool steels, NbC serves either as a grain refiner or as a hard phase contributing to the enhancement of wear resistance.^[33] It also restrains the grain growth and improves the hot hardness. Similar effects are caused by Nb(C,N) precipitates in N-bearing steels, though Nb(C,N) can also be considered as a deleterious precipitate when formed in a fine form at the austenite grain boundaries. Particularly, a high cooling rate tends to decrease the precipitate size and thus also ductility. On the other

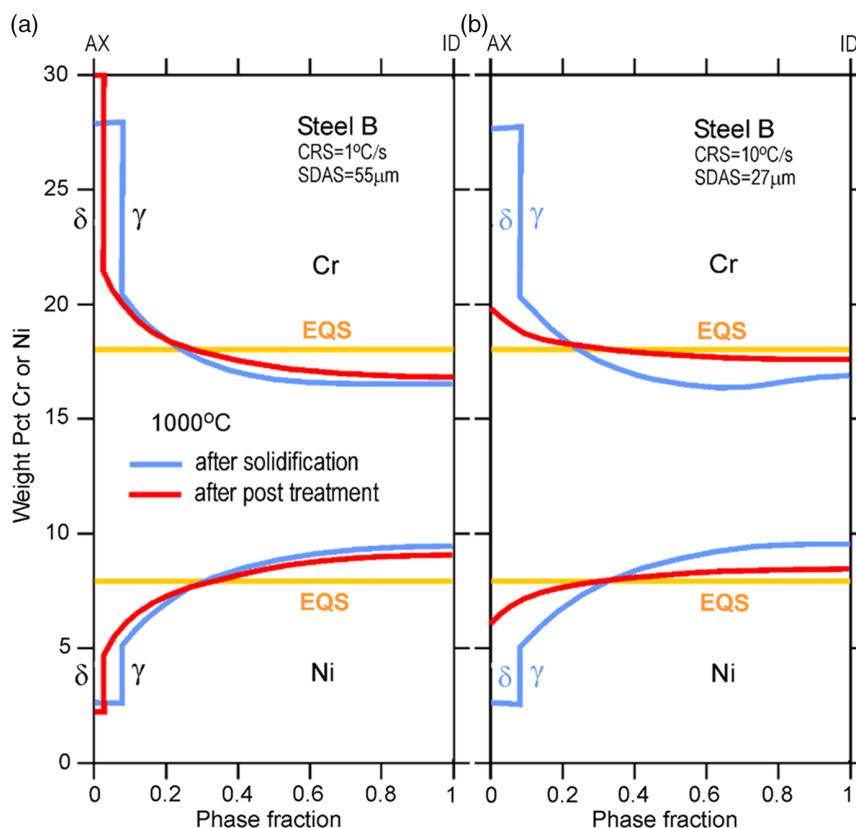


Figure 11. Calculated concentration profiles at $1000^\circ C$ for Cr and Ni in steel B (Table 1) solidified at the rates of a) $CRS = 1^\circ C s^{-1}$ and b) $CRS = 10^\circ C s^{-1}$, heated at $5^\circ C s^{-1}$, held for 60 min at $1200^\circ C$, and cooled at $1^\circ C s^{-1}$.

hand, the precipitation of Nb(C,N) is influenced also by other alloying. According to Vedani et al.,^[34] coarse TiN or Ti(C,N) particles formed earlier in the steel can act as preferential nucleation sites for Nb(C,N) so that these new particles can grow coarse enough to be able to cause reduction of ductility significantly. Nevertheless, if the Ti(C,N) particles are fine themselves, the ductility could also deteriorate as a result of Ti alloying.^[35] Post-treatment calculations of SOL are presented in the following to see their influence on the precipitation and dissolution of NbC and Nb(C,N) in the solid steel. Also considered is the effect of Ti alloying on the amount of Nb(C,N), though only from the thermodynamic point of view, that is, to show the extent to which the Ti(C,N) particles formed already in the mushy zone could consume C and N from the latter, thereby precipitating Nb(C,N) particles. Again, no experimental measurements are available for these example calculations, but two continuous cooling precipitation (CCP) curve validations for Nb(C,N) have been presented in Section 4.8. In addition, several equilibrium condition calculations on the austenite–carbonitride equilibria in low-alloyed steels have been validated with the corresponding measurements, in the study by Miettinen et al.^[36]

Figure 12 shows the calculated amounts of NbC in steel A solidified at two rates (CRS = 1 °C s^{−1} and CRS = 10 °C s^{−1}) going through two different post-treatments: heating at 0.5 °C s^{−1} and holding for 20 min at 1100 °C (red curves) and heating at 10 °C s^{−1} and holding for 2 min at 1200 °C (blue curves). In both cases, the final cooling rate is assumed to be 10 °C s^{−1}. It is to be noted that after solidification, the

temperature of the primary NbC precipitation was higher than that of equilibrium precipitation (EQP). This is due to the enrichment of Nb in the interdendritic regions, in a real solidification process. Even the incubation was insufficient to lower that temperature below its equilibrium value. In addition, the amounts of NbC precipitates remained much smaller than predicted by the EQP, preliminarily due to the finite kinetics of the former.

It is important to understand now the effect of post-treatment processes of 1100 °C. In the coarser structure (SDAS = 132 μm), the long-duration post-treatment (20 min) doubles the amount of NbC in comparison with that of the as-cast case. The increased amount of NbC is due to the solute flow (diffusion) to the γ/NbC phase interface from its austenitic surroundings, as the interface is impoverished by the solutes during the as-cast formation of NbC. Another reason promoting the NbC formation is because the holding temperature of 1100 °C still lies below the temperature of EQP. This suggests that at 1100 °C, NbC has still some driving force to grow, particularly, as there is enough time for its growth. In the finer structure (SDAS = 66 μm), the corresponding NbC amount is even greater, that is, about four times higher than the as-cast case. This is due to the shorter diffusion distances, thus enhancing the solute flow to the γ/NbC phase interface.

Next, we make a view on the effect of post-treatment at 1200 °C. In the coarser dendritic structure (SDAS = 132 μm), the short-duration post-treatment makes NbC disappear within just 2 min. This is because of the strong driving force for the NbC dissolution, as the temperature of 1200 °C is now above the temperature of its EQP. Consequently, during the final

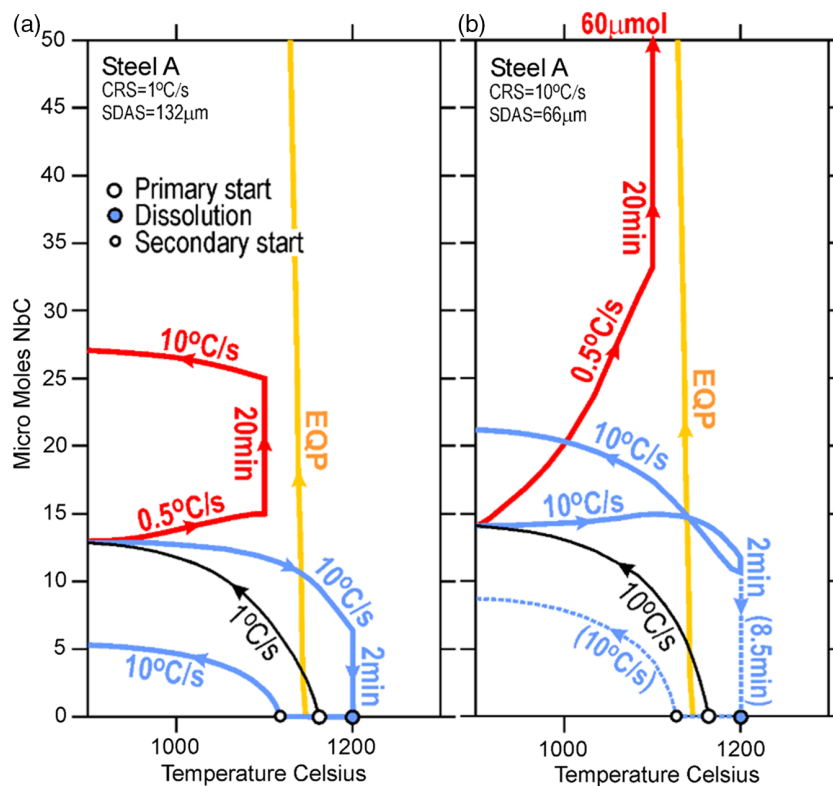


Figure 12. Calculated amounts of NbC in steel A (Table 1) solidified at the rates of a) CRS = 1 °C s^{−1} and b) CRS = 10 °C s^{−1} and heated, held, and cooled, as shown by the data of the red and blue curves.

cooling with a high rate of $10^{\circ}\text{C s}^{-1}$, NbC forms again, but at some lower temperature. This is due not only to the strong incubation occurring at that cooling rate but also due to the lowered interdendritic solute compositions, following the effective post-treatment at high temperature. In addition, because of the shorter time for solute diffusion, the amount of NbC remains smaller than in the as-cast case. In the finer structure (SDAS = $66\text{ }\mu\text{m}$), the short holding time of 2 min was just not enough to dissolve NbC from the structure. This is due to the stronger tendency of the short diffusion distances (at this higher temperature) to enhance the solute flow to the γ/NbC interface so that not even the increased driving force of NbC dissolution can compensate it. Nevertheless, by increasing the holding time to 8.5 min, the solute flow to the γ/NbC interface finally ceases so that the driving force “starts to work again,” to complete the NbC dissolution (see blue broken lines).

The previous calculations showed some alternative ways to control the precipitate amounts by post-treatment. However, the type of treatment chosen, of course, always depends on whether the presence of the precipitate is desired or not. If the presence of NbC is desired, as in tool steel applications, one should avoid making those post-treatments that dissolve NbC too much. Typically, long post-treatments at sufficiently low temperatures tend to increase the amount of NbC, which might be too low in the as-cast structure. This, of course, depends on the alloying type and contents also. Particularly, if steel

contains a detectable amount of nitrogen, carbonitride Nb(C,N) will form instead of just NbC. The precipitation behavior of Nb(C,N) is somewhat different and depends on the nitrogen level of the steel. A high N composition can considerably raise the formation temperature of Nb(C,N) and increase its final amount. This is not any problem, if the presence of Nb(C,N) is desired and/or allowed in the steel. However, Nb(C,N) precipitation can also be considered deleterious, particularly as fine networks along the austenite grain boundaries. The next example introduces the treatments, which could be used to avoid the Nb(C,N) formation in steels. Due to the high cooling rate applied in these calculations, these can be used to illustrate the problematic formation of Nb(C,N) at the rapidly cooling surfaces of continuous casting strands.

Figure 13 shows the effect of N and Ti alloying on the amounts of NbC or Nb(C,N) at 900°C formed in steel A held for 2 min and 8 min at various temperatures. The cooling and heating rates of these calculations were $10^{\circ}\text{C s}^{-1}$. The addition of 0.01 wt% N considerably increases the amount of Nb(C,N) (red curves) in regard to that of NbC of the base steel (green curves). This is, of course, due to the nitrogen tied up in Nb(C,N). Adding 0.03 wt% Ti to that alloy, however, decreases the amount of Nb(C,N) (blue curves), as most of the nitrogen is then tied up to carbonitride Ti(C,N) formed already in the mushy zone. However, the level of the low amounts of NbC cannot still be achieved. The benefit, however, may be that the Nb(C,N) particles

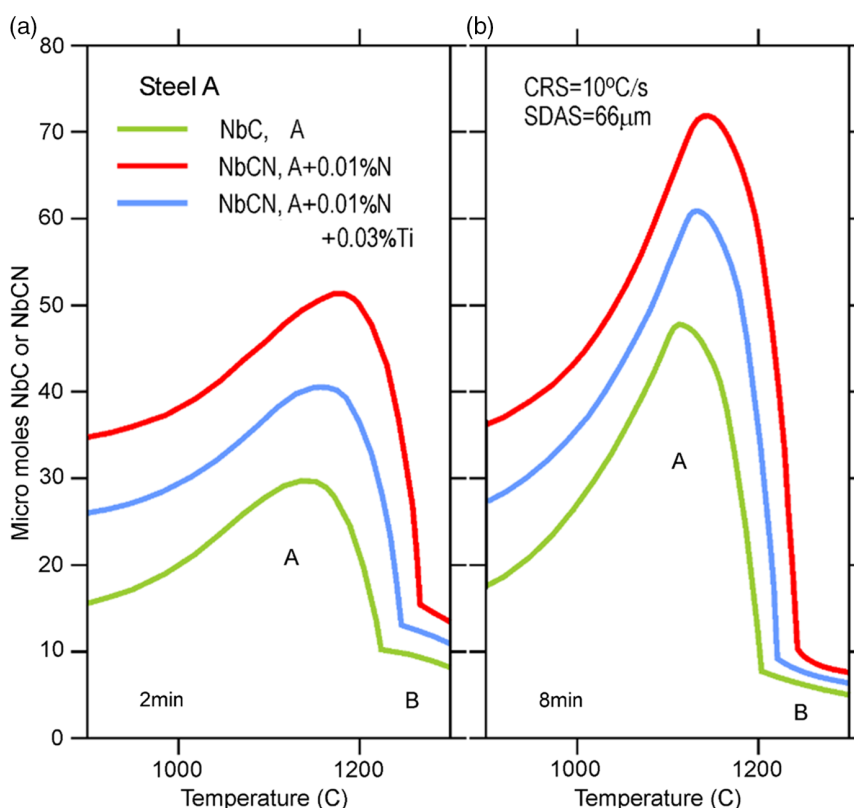


Figure 13. Calculated amounts of NbC or Nb(C,N) at 900°C in three low-alloyed steels held for a) 2 min and b) 8 min at various temperatures. The cooling rate of solidification (down to 900°C), the heating rate up to the holding temperature, and the cooling rate after holding were $10^{\circ}\text{C s}^{-1}$. A = as-cast precipitates not dissolved and B = as-cast precipitates dissolved.

can now precipitate on the Ti(C,N) particles in a coarser form making the steel less brittle. Nevertheless, the amounts of Ti(C,N) formed in this case are quite high (about 500 μm) and if formed as fine particles, they can deteriorate the steel structure even more.

Finally, let us consider the effect of post-treatment itself. With both holding times, 2 and 8 min, the amounts of NbC or Nb(C,N) increase with the increasing holding temperature. This is due to the previously stated increased solute flow from austenite to the γ /precipitate phase interface. That flow is particularly strong in the fine dendritic structure (SDAS = 66 μm) obtained at the solidification rate of 10 $^{\circ}\text{C s}^{-1}$. During the longer holding treatment (8 min), the precipitate amounts, of course, become much higher than those during the shorter holding treatment (2 min), but only in region A, where the original as-cast precipitates are not yet dissolved. In region B, instead, the driving force for the precipitate dissolution becomes so high that the as-cast precipitates will be completely dissolved. So, the relatively smaller precipitate amounts obtained in region B represent only the final-stage precipitates formed during final cooling. In Figure 13b, note the lower amounts of final-stage precipitates obtained after the 8 min holding. This indicates that the 2 min holding was not yet sufficient to get uniform solute compositions in austenite, which would stop the precipitate dissolution at a constant temperature. Even the 8 min time is not adequate for that, but it is so close anyway that there is no clear benefit of increasing the holding time even more, particularly because this could promote the grain growth at such high temperatures. The main result of the present calculations is that by a proper post-treatment, one can reduce the amounts of some unwanted precipitates formed after solidification. However, there is no specific use of performing these calculations for precipitates that form at high temperatures. Typical precipitates or inclusions that cannot be dissolved are carbonitride Ti(C,N) and sulfide (Fe,Mn)S, if they form, as normally from the liquid state. For most carbides (such as M_{23}C_6) and AlN, instead, the post-treatment calculations work well. And, of course, we must remember the role of alloying in these calculations. Even a slight change in the composition of the solute, which is tied up in the precipitate, can change the results. As an example, to drop the position of the red curves close to that of the green curves in Figure 13, we must decrease the Nb or C composition of the red-curve steel with 0.005 or 0.02 wt%, respectively.

4. Validation of SOL Calculations with Solidification Measurements

This section shows a comparison between SOL calculations and actual experimental solidification data obtained for some steels. The experimental data come from the differential thermal analysis (DTA) measurements of the liquidus, austenite formation, zero-strength, and solidus temperatures, as well as from the electron microprobe (EMP) measurements of solute microsegregation and solute partitioning between ferrite and austenite. In addition, calculated residual ferrite amounts, CCP curves of certain precipitates, SDAS, and austenite grain sizes are compared with the experimental or predicted values.

Table 2. Average deviation between experimental and calculated liquidus temperatures of ternary iron alloys.

| Ternary alloy | System | Number of alloys | ΔT_{avg} [$^{\circ}\text{C}$] | Reference(s) |
|---|----------|------------------|--|--------------|
| Carbon alloys | Fe–Al–C | 20 | 4.0 | [37–39] |
| 283 alloys $\Delta T_{\text{avg}} = 5.6^{\circ}\text{C}$ | Fe–Cr–C | 114 | 4.8 | [38,40–42] |
| | Fe–Cu–C | 21 | 3.9 | [43,44] |
| | Fe–Mn–C | 18 | 12.0 | [45,46] |
| | Fe–Mo–C | 14 | 4.4 | [47] |
| | Fe–Ni–C | 44 | 5.4 | [48,49] |
| | Fe–Si–C | 38 | 6.6 | [50–53] |
| | Fe–V–C | 14 | 8.2 | [54] |
| | Fe–Cr–Al | 15 | 6.7 | [55,56] |
| Cr and Ni alloys 274 alloys $\Delta T_{\text{avg}} = 3.9^{\circ}\text{C}$ | Fe–Cr–Cu | 9 | 12.5 | [57] |
| | Fe–Cr–Mn | 17 | 0.6 | [58,59] |
| | Fe–Cr–Mo | 9 | 5.9 | [60,61] |
| | Fe–Cr–Ni | 126 | 1.1 | [62–65] |
| | Fe–Cr–Si | 8 | 9.3 | [66] |
| | Fe–Cr–Ti | 9 | 8.3 | [67] |
| | Fe–Ni–Cu | 12 | 12.6 | [68,69] |
| | Fe–Ni–Mn | 24 | 0.9 | [58,59] |
| Other alloys 55 alloys $\Delta T_{\text{avg}} = 11.8^{\circ}\text{C}$ | Fe–Ni–Mo | 20 | 12.0 | [70] |
| | Fe–Ni–Ti | 25 | 3.9 | [71] |
| | Fe–Mn–Al | 4 | 8.4 | [72] |
| | Fe–Mn–Cu | 3 | 8.6 | [73] |
| | Fe–Mn–Si | 15 | 22.9 | [74] |
| | Fe–Mo–Cu | 7 | 12.2 | [75] |
| | Fe–Mo–Si | 4 | 9.1 | [76] |
| | Fe–Si–Al | 11 | 7.7 | [77,78] |
| | Fe–Cu–Al | 11 | 3.9 | [79] |

4.1. Liquidus Temperature

From all phase-change temperatures, the liquidus temperature can be most accurately measured. Table 2 and 3 show the average deviation (T_{avg}) obtained between the experimental^[22,37–112] and calculated liquidus temperatures for 283 ternary Fe–X–C alloys (Table 2), 274 ternary Fe–Cr–X and Fe–Ni–X alloys (Table 2), 55 ternary Fe–X–Y alloys (Table 2), as well as 410 low-alloyed (143) and high-alloyed (267) steels (Table 3). The average deviations in the predicted liquidus temperatures are 5.6 $^{\circ}\text{C}$ for carbon alloys, 3.9 $^{\circ}\text{C}$ for Cr and Ni alloys, and 11.8 $^{\circ}\text{C}$ for other alloys (Table 2), while the average deviation for the low- and high-alloyed steels was 3.2 $^{\circ}\text{C}$ (see Table 3). Table 4 shows the average deviation obtained with the liquidus temperature equations given in the literature.^[94,113–116] The experimental data are the same as in Table 3. As can be seen, the deviations by these equations are clearly larger than those predicted by SOL. The liquidus temperatures were also compared with those measured experimentally for cast irons. In this case, the average deviation for 57 alloys taken from other studies^[50,51,94,117–126] was 7.5 $^{\circ}\text{C}$.

Table 3. Average deviation between experimental and calculated liquidus temperatures of low-alloyed (L) and high-alloyed (H) steels.

| Steel type | Number of alloys | ΔT_{avg} [°C] | Reference(s) |
|------------|------------------|------------------------------|--------------|
| L + H | 40 | 3.4 | [22] |
| L | 29 | 0.9 | [53] |
| L + H | 23 | 1.1 | [58,59] |
| L + H | 6 | 0.8 | [62] |
| H | 29 | 3.1 | [80] |
| L + H | 20 | 4.1 | [81] |
| H | 10 | 3.6 | [82] |
| L | 7 | 3.5 | [83] |
| H | 3 | 6.6 | [84] |
| H | 5 | 5.6 | [85] |
| H | 4 | 4.9 | [86] |
| H | 3 | 2.8 | [87] |
| H | 9 | 2.0 | [88] |
| H | 6 | 3.9 | [89] |
| H | 2 | 9.5 | [90] |
| H | 12 | 5.3 | [91] |
| L | 5 | 2.0 | [92] |
| H | 6 | 5.1 | [93] |
| L + H | 88 | 3.8 | [94] |
| H | 10 | 2.6 | [95] |
| H | 18 | 1.7 | [96] |
| H | 24 | 3.0 | [97] |
| L | 6 | 3.4 | [98] |
| L | 3 | 1.1 | [99] |
| H | 3 | 1.1 | [100] |
| H | 3 | 1.5 | [101] |
| H | 3 | 6.3 | [102] |
| H | 1 | 6.1 | [103] |
| L | 1 | 2.4 | [104] |
| L | 1 | 0.3 | [105] |
| H | 4 | 3.7 | [106] |
| H | 3 | 5.4 | [107] |
| H | 2 | 3.0 | [108] |
| L | 2 | 6.8 | [109] |
| L | 2 | 3.5 | [110] |
| L | 2 | 4.4 | [111] |
| H | 15 | 3.9 | [112] |
| Low alloy | 143 | 3.0 | Total |
| High alloy | 267 | 3.3 | Total |
| All steels | 410 | 3.2 | Total |

4.2. Austenite Formation Temperature

In steels, austenite starts to form as a primary phase from liquid or as a secondary phase from liquid (start of peritectic transformation) or from ferrite below the solidus

Table 4. The average deviation between experimental and calculated liquidus temperatures of low-alloyed and high-alloyed steels using literature equations and SOL.

| Steel type | Number of alloys | ΔT_{avg} [°C] | | | | | SOL |
|------------|------------------|------------------------------|-------|-------|-------|-------|-----|
| | | [94] | [113] | [114] | [115] | [116] | |
| Low alloy | 143 | 4.8 | 6.3 | 5.1 | 8.0 | 6.0 | 3.0 |
| High alloy | 267 | 36.8 | 6.3 | 12.8 | 15.1 | 15.8 | 3.3 |

Table 5. The average deviation between experimental and calculated austenite formation temperatures of low-alloyed (L) and high-alloyed (H) steels.

| Steel type | Number of alloys | ΔT_{avg} [°C] | Reference |
|--------------|------------------|------------------------------|-----------|
| L | 9 | 2.8 | [22] |
| H | 16 | 11.8 | [22] |
| H | 3 | 8.6 | [82] |
| L | 6 | 4.0 | [83] |
| H | 2 | 2.3 | [84] |
| H | 1 | 2.5 | [87] |
| L | 4 | 3.1 | [92] |
| H | 6 | 10.6 | [95] |
| L | 2 | 4.5 | [109] |
| L | 2 | 5.5 | [110] |
| L | 2 | 3.2 | [111] |
| Low alloyed | 25 | 3.5 | Total |
| High alloyed | 28 | 10.2 | Total |
| All steels | 53 | 7.0 | Total |

temperature (start of δ/γ transformation). In this presentation, only the two latter cases are considered (the first case was considered in connection with the liquidus temperatures). **Table 5** shows the deviation obtained between the experimental^[22,82–84,87,92,95,109–111] and calculated austenite formation temperatures for 25 low-alloyed and 28 high-alloyed (stainless) steels. The average deviation between the calculated and the measured temperatures was 7.0 °C. Also shown are the alloy number and the average deviation for each reference. Due to the poorer accuracy of the temperature measurements for secondary phases than for primary phases (i.e., for the liquidus temperatures), the agreement can still be considered reasonable. For instance, by applying the EQS mode in calculations (i.e., infinitely rapid solute diffusion), the average deviation increases to 9 °C.

4.3. Zero-Strength Temperature

A local strengthening in the solidifying microstructure can be assumed to start at a solid fraction value of $f_s = 0.75$,^[127] which represents a median value of two other reported values, that is, $f_s = 0.7$ by Shin et al.^[128] and $f_s = 0.8$ by Yamanaka et al..^[129] The corresponding temperature, related to the solid fraction of $f_s = 0.75$, is obtained from the SOL calculation. **Table 6** shows

Table 6. The average deviation between experimental and calculated zero-strength temperatures of low-alloyed (L) steels.

| Steel type | Number of alloys | ΔT_{avg} [°C] | Reference |
|------------|------------------|------------------------------|-----------|
| L | 3 | 3.2 | [99] |
| L | 6 | 5.5 | [128] |
| L | 15 | 6.4 | [130] |
| L | 1 | 0.3 | [131] |
| Low alloy | 25 | 5.6 | Total |

the deviation obtained between the experimental^[99,128,130,131] and the calculated zero-strength temperatures for 25 low-alloyed steels. The average deviation between the calculated and the measured temperatures is 5.6 °C. Also shown are the alloy number and the average deviation for each reference. Knowing the difficulties of the measuring technique and the approximate criterion for the start of the strengthening ($f_s = 0.75$), the agreement can be considered reasonable.

4.4. Solidus Temperature

The measuring accuracy of thermal analysis is poorer for solidus temperatures than for liquidus temperatures. The solidus is associated with the minimum of the cooling rate curve of the sample, but this minimum may sometimes be difficult to locate. Particularly, this is the case if the heat is released by some other transformations close to the solidus temperature. **Table 7** shows the deviation obtained between the experimental^[22,52,82,84,86–88,90,92,93,95,96,99,102–111,128,130–132] and calculated solidus temperatures for 75 low-alloyed and 103 high-alloyed (stainless) steels. The average deviation between the calculated and the measured temperatures is as high as 10.3 °C but due to the aforementioned poor accuracy in the measuring technique, the correlation can be considered reasonable. Also shown are the alloy number and the average deviation for each reference. By applying the EQS mode in calculations (i.e., infinitely rapid solute diffusion), the average deviation increases to 14.7 °C.

Table 8 shows the average deviations obtained by the solidus temperature equations of the literature.^[94,115,116] The experimental data is the same as in Table 7. As shown, the deviations by these equations are larger than those predicted by SOL. The solidus temperatures were also compared with those measured for cast irons. In this case, the average deviation for 52 alloys from other studies^[50,51,117–126] was 6.6 °C. Note that these measurements may have been related also to the eutectic temperature, due to the difficulty of distinguishing the corresponding DTA information of solidus from the eutectic.

4.5. Solute Microsegregation and Partition

Solute microsegregation and partition have been studied by EMP analysis of the samples quenched from just below the solidus temperature.^[22,86] Mean solute concentrations were evaluated in the dendrite center areas (D) and the interdendritic areas (ID) of the samples. The microsegregation ratio is defined as

Table 7. The average deviation between experimental and calculated solidus temperatures of low-alloyed (L) and high-alloyed (H) steels.

| Steel type | Number of alloys | ΔT_{avg} [°C] | Reference |
|------------|------------------|------------------------------|-----------|
| L | 16 | 8.1 | [22] |
| H | 24 | 11.4 | [22] |
| L | 24 | 7.8 | [52] |
| H | 10 | 14.7 | [82] |
| H | 3 | 1.9 | [84] |
| H | 4 | 10.9 | [86] |
| H | 3 | 8.2 | [87] |
| H | 9 | 15.8 | [88] |
| H | 3 | 9.1 | [90] |
| L | 2 | 15.4 | [92] |
| H | 6 | 8.1 | [93] |
| H | 8 | 14.5 | [95] |
| H | 16 | 10.2 | [96] |
| L | 3 | 22.0 | [99] |
| H | 3 | 6.8 | [101] |
| H | 3 | 14.8 | [102] |
| H | 1 | 0.8 | [103] |
| L | 1 | 6.6 | [104] |
| L | 1 | 2.0 | [105] |
| H | 4 | 5.6 | [106] |
| H | 3 | 10.2 | [107] |
| H | 2 | 8.6 | [108] |
| L | 2 | 2.4 | [109] |
| L | 2 | 5.5 | [110] |
| L | 2 | 4.5 | [111] |
| L | 6 | 12.0 | [128] |
| L | 15 | 11.3 | [130] |
| L | 1 | 9.8 | [131] |
| H | 1 | 6.7 | [132] |
| Low alloy | 75 | 9.3 | Total |
| High alloy | 103 | 11.1 | Total |
| All steels | 178 | 10.3 | Total |

Table 8. The average deviation between experimental and calculated solidus temperatures of low-alloyed and high-alloyed steels using literature equations and SOL.

| Steel | Number of alloys | ΔT_{avg} [°C] | | | |
|------------|------------------|------------------------------|-------|-------|------|
| | | [94] | [115] | [116] | SOL |
| Low alloy | 75 | 16.5 | 43.1 | 18.2 | 9.3 |
| High alloy | 103 | 34.3 | 58.9 | 65.4 | 11.1 |

$I_i = C_i^{\text{ID}}/C_i^{\text{D}}$, where C_i^{ID} is the mean solute (i) concentration in the interdendritic area and C_i^{D} is the mean solute (i) concentration in the dendrite centre area. The partition ratios are defined as $P_i^{\delta/\gamma-D} = C_i^{\delta\text{D}}/C_i^{\gamma\text{D}}$ and $P_i^{\epsilon/\gamma-ID} = C_i^{\epsilon\text{ID}}/C_i^{\gamma\text{ID}}$, where

C_i^X is the mean solute concentration in ferrite ($\varphi = \delta, \epsilon$) or austenite ($\varphi = \gamma$) in the dendrite area ($X = D$) or the interdendritic area ($X = ID$). Table 9 shows the comparison obtained between the experimental^[22,86] and calculated average values of microsegregation and partition ratios for certain solutes in low-alloyed and stainless steels. The calculated partition ratios of Cr and Ni agree well with the measured values but in the case of microsegregation, the agreement is poor. This may not only be due to the uncertainty in the measuring technique based on the line analysis (as the line may not always pass through the dendrite center area) but also due to the uncertainty caused by the effect of possible formation of inclusions and interdendritic eutectic ferrite on the measured values regardless of whether their solute compositions are included in the analysis. For Si, however, the calculations show a systematically lower tendency of microsegregation (typical I_{Si} values are between 1 and 1.5) than observed in the measurements (typical I_{Si} values are between 1.2 and 2). This is difficult to explain since the well-validated thermodynamic and diffusion data of the SOL module suggest only a low microsegregation tendency for Si.

4.6. Residual Ferrite Amounts of Stainless Steels

The control of the residual ferrite amount in stainless steel castings is of great importance when aiming at a good product quality. Table 10 shows the calculated (SOL), experimental,^[22,31,85,97,133–136] and predicted^[137] residual ferrite amounts in numerous stainless steels. As shown at the bottom of Table 10, the average deviation between the calculations and the experimental measurements is 1.12 pct and that deviation

Table 9. Calculated and experimental average values of microsegregation ratios $I_i = C_i^D/C_i^D$ and partition ratios of $P_i^{\delta/\gamma-D} = C_i^{\delta}/C_i^{\gamma}$ and $P_i^{\epsilon/\gamma-ID} = C_i^{\epsilon}/C_i^{\gamma}$ in some low-alloyed (series 200) and stainless (series 400) steels. The cooling rate in calculations and measurements was 0.5°C s^{-1} .

| Series | Number of alloys | Ratio | Value | | |
|--------|------------------|-------------------------------|--------------|------------|-----------|
| | | | Experimental | Calculated | Reference |
| 200 | 8 | I_{Cr} | 1.67 | 1.25 | [22] |
| 200 | 5 | I_{Ni} | 1.34 | 1.29 | [22] |
| 200 | 6 | I_{Mn} | 1.61 | 1.36 | [22] |
| 200 | 3 | I_V | 1.97 | 1.77 | [22] |
| 400 | 14 | I_{Cr} | 1.14 | 1.28 | [22] |
| 400 | 14 | I_{Ni} | 1.24 | 1.26 | [22] |
| 400 | 14 | I_{Mn} | 1.59 | 1.50 | [22] |
| 400 | 4 | I_{Mo} | 2.17 | 1.83 | [22] |
| 400 | 4 | I_{Cr} | 1.00 | 1.00 | [86] |
| 400 | 1 | I_{Ni} | 1.20 | 1.06 | [86] |
| 400 | 4 | I_{Mo} | 1.10 | 1.05 | [86] |
| 400 | 5 | $P_{Cr}^{\delta/\gamma-D}$ | 1.22 | 1.21 | [22] |
| 400 | 4 | $P_{Ni}^{\delta/\gamma-D}$ | 0.69 | 0.72 | [22] |
| 400 | 4 | $P_{Cr}^{\epsilon/\gamma-ID}$ | 1.17 | 1.16 | [22] |
| 400 | 4 | $P_{Ni}^{\epsilon/\gamma-ID}$ | 0.75 | 0.73 | [22] |

between the calculations and the predictions^[137] is 2.40 pct. The agreement is reasonably good in both cases. The agreement, however, seems to get worse if the steel contains significant fractions of ferrite, like in the case of duplex stainless steels. In such cases, the calculated ferrite amounts remain smaller. As an example, the calculated ferrite amounts for eight duplex stainless steels reported by Glowina et al.^[138] are only 50–90 pct of their measured values. On the other hand, the nitrogen compositions of these steels were very high (even 0.3 wt%). Hence, part of that nitrogen may have formed N_2 gas because of the presence of pores in the solid structure. In such a case, the expected effect of nitrogen to stabilize austenite decreases and the residual ferrite fraction remains higher. Additional validations for the calculated residual ferrite amounts are given in Figure 14 and 15. In the case of post-treated steels (Figure 15), note the delayed disappearance of the last ferrite particles according to the measurements. By calculations, ferrite disappears straightforwardly, but the agreement is still reasonable.

4.7. CCP Curves of Some Precipitates

Measurements have been included in other studies^[139–143] to construct the CCP curves for AlN, (Fe,Mn)S, Nb(C,N), and Sigma. The calculated CCP curves agree reasonably well with these measurements, as shown in Figure 16–18. In the case of Figure 18, it is to be noted that the sigma phase did not form at the grain boundary but at the δ/γ phase interface. This indeed is a typical characteristic of sigma phase.^[144] Note also the sluggish way sigma will form, in comparison with the other precipitates, AlN, (Fe,Mn)S, and Nb(C,N). An additional validation was carried out by comparing the SOL calculations with the CCP-type carbide formation temperatures for six high-carbon steels from Rose and Hougardy^[145] and seven high-carbon steels from van der Voort.^[146] The results have been presented in earlier work.^[147] The average deviation between the measured and calculated carbide formation temperatures was 16.5°C . The agreement is reasonable, considering the complex process history before the carbide formation and the somewhat moderate accuracy in measuring the first tiny particles of the carbides.

4.8. Microstructure Data

As stated earlier, the SDAS calculations can be given by the user or they can be calculated by the SOL module, depending on the applied cooling rate of the solidification process. For the calculation of SDAS, a specific regression equation was optimized. Figure 19 shows the validation of this equation with the measurements available in the literature.^[22,26,45,85,87,90,98,148–160] The agreement can be considered reasonable, considering the difficulty in measuring good average values for the dendrite arm spacing from the quenched samples. A similar optimization was made to calculate the austenite grain growth during the cooling process after solidification. Figure 20 shows a comparison of the calculated and measured^[10,161–169] austenite grain sizes in several low-alloyed steels. Again, due to the uncertainty of measuring good average values for the grain sizes, the obtained agreement can be considered reasonable. In both calculation algorithms for the SDAS as well as the austenite grain size,

Table 10. Calculated (SOL), experimental,^[22,31,85,97,133–136] and predicted^[137] residual ferrite amounts in stainless steels. CRT denotes the cooling rate.

| Ref. | Composition [wt%] | | | | | | | | | | CRT [°C s ⁻¹] | Ferrite [pct] | | |
|------|-------------------|------|------|-------|------|-------|------|-----|-----|-----|---------------------------|---------------|-------|-------|
| | C | Si | Mn | Cr | Mo | Ni | N | Cu | Nb | Ti | | Calc. | Exp. | Pred. |
| [22] | .012 | .31 | 1.76 | 19.80 | .10 | 9.90 | .031 | – | – | – | .50 | 9.47 | 9.00 | 7.19 |
| | .019 | .31 | .94 | 19.50 | .11 | 10.20 | .044 | – | – | – | .50 | 5.64 | 5.80 | 5.59 |
| | .036 | .44 | 1.25 | 18.40 | .38 | 9.10 | .081 | .20 | – | – | .50 | 3.64 | 2.00 | 2.50 |
| | .068 | .59 | 1.44 | 17.20 | .47 | 10.30 | .005 | – | – | .51 | .50 | 4.10 | 4.10 | 4.08 |
| | .052 | .44 | 1.71 | 17.20 | 2.80 | 12.60 | .010 | – | .54 | – | .50 | 1.92 | 2.90 | 4.04 |
| | .023 | .53 | 1.58 | 17.20 | 2.63 | 13.50 | .031 | .19 | – | – | .50 | 1.63 | 3.50 | 0.83 |
| | .048 | .63 | 1.65 | 17.70 | 2.68 | 13.40 | .045 | .15 | – | – | .50 | 1.80 | 0.10 | 0.26 |
| | .024 | .58 | 1.79 | 17.40 | 2.77 | 12.80 | .200 | .03 | – | – | .50 | 0.29 | 0.10 | – |
| | .008 | .24 | 1.77 | 25.10 | 2.30 | 22.20 | .067 | – | – | – | .50 | 0.25 | 0.70 | – |
| | .130 | .52 | 1.67 | 24.30 | .11 | 20.50 | .053 | – | – | – | .50 | 0.53 | 0.40 | – |
| [31] | .059 | .70 | .92 | 18.49 | .08 | 8.84 | .047 | – | – | – | .40 | 3.81 | 4.90 | 4.73 |
| | .059 | .70 | .92 | 18.49 | .08 | 8.84 | .047 | – | – | – | 16.00 | 4.47 | 3.90 | 4.73 |
| [85] | .004 | .70 | .57 | 20.40 | – | 8.00 | .013 | – | – | – | .94 | 13.71 | 12.60 | 28.24 |
| | .004 | .70 | .57 | 20.40 | – | 8.00 | .013 | – | – | – | 5.90 | 14.12 | 13.50 | 28.24 |
| | .004 | .70 | .57 | 20.40 | – | 8.00 | .013 | – | – | – | 44.00 | 17.68 | 16.40 | 28.24 |
| | .005 | .80 | .77 | 19.70 | – | 10.90 | .011 | – | – | – | .42 | 5.50 | 5.50 | 8.81 |
| | .005 | .80 | .77 | 19.70 | – | 10.90 | .011 | – | – | – | 4.00 | 5.73 | 6.70 | 8.81 |
| | .005 | .80 | .77 | 19.70 | – | 10.90 | .011 | – | – | – | 32.00 | 5.93 | 8.40 | 8.81 |
| | .015 | .86 | .70 | 18.00 | – | 12.00 | .012 | – | – | – | .54 | 0.79 | 1.50 | 1.59 |
| | .015 | .86 | .70 | 18.00 | – | 12.00 | .012 | – | – | – | 3.60 | 0.87 | 1.18 | 1.59 |
| | .015 | .86 | .70 | 18.00 | – | 12.00 | .012 | – | – | – | 15.00 | 0.90 | 1.14 | 1.59 |
| | .015 | .86 | .70 | 18.00 | – | 12.00 | .012 | – | – | – | 35.00 | 0.95 | 1.10 | 1.59 |
| | .006 | .17 | .05 | 19.10 | – | 6.30 | .016 | – | – | – | .72 | 13.45 | 13.50 | 34.35 |
| | .006 | .17 | .05 | 19.10 | – | 6.30 | .016 | – | – | – | 4.30 | 13.66 | 15.20 | 34.35 |
| | .006 | .17 | .05 | 19.10 | – | 6.30 | .016 | – | – | – | 32.00 | 16.19 | 16.70 | 34.35 |
| | .006 | .17 | .05 | 19.10 | – | 6.30 | .016 | – | – | – | 47.00 | 17.69 | 18.00 | 34.35 |
| [97] | .043 | 2.11 | 1.56 | 19.10 | – | 12.10 | .032 | – | – | – | 2.00 | 1.45 | 3.50 | 4.49 |
| | .027 | 2.10 | 1.62 | 19.20 | – | 13.10 | .029 | – | – | – | 2.00 | 1.72 | 2.00 | 3.68 |
| | .040 | 1.91 | 1.63 | 19.20 | – | 14.10 | .033 | – | – | – | 2.00 | – | – | – |
| | .030 | 2.18 | 1.58 | 19.20 | – | 15.10 | .030 | – | – | – | 2.00 | 0.43 | – | – |
| | .026 | 1.91 | 1.54 | 19.00 | – | 16.10 | .030 | – | – | – | 2.00 | 0.18 | – | – |
| | .025 | .60 | 1.51 | 22.00 | – | 12.00 | .044 | – | – | – | 2.00 | 5.60 | 9.80 | 6.40 |
| | .024 | .52 | 1.52 | 22.10 | – | 13.00 | .041 | – | – | – | 2.00 | 3.73 | 7.40 | 4.63 |
| | .029 | .53 | 1.62 | 22.10 | – | 14.00 | .045 | – | – | – | 2.00 | 1.24 | 4.80 | 1.91 |
| | .022 | .53 | 1.59 | 22.10 | – | 15.00 | .041 | – | – | – | 2.00 | 1.24 | 1.50 | 0.30 |
| | .028 | .53 | 1.51 | 21.80 | – | 16.00 | .038 | – | – | – | 2.00 | 0.81 | – | – |
| | .027 | .58 | 1.62 | 25.30 | – | 16.10 | .053 | – | – | – | 2.00 | 3.84 | 7.80 | 4.16 |
| | .042 | .58 | 1.55 | 25.30 | – | 17.10 | .054 | – | – | – | 2.00 | 1.53 | 3.70 | 1.52 |
| | .025 | .54 | 1.56 | 25.10 | – | 18.10 | .055 | – | – | – | 2.00 | 1.42 | 1.30 | – |
| | .025 | .56 | 1.53 | 25.30 | – | 19.10 | .052 | – | – | – | 2.00 | 1.15 | 0.50 | – |
| | .019 | .43 | 1.41 | 18.40 | – | 9.50 | .033 | – | – | – | 2.00 | 3.99 | 5.20 | 4.88 |
| | .017 | .36 | 1.42 | 18.80 | – | 9.50 | .100 | – | – | – | 2.00 | 1.86 | 2.40 | 1.14 |
| | .020 | .42 | 1.33 | 18.50 | – | 9.50 | .146 | – | – | – | 2.00 | 0.47 | 0.70 | – |
| | .022 | .54 | 1.54 | 17.50 | 2.56 | 11.00 | .033 | – | – | – | 2.00 | 5.06 | 6.60 | 7.26 |
| | .022 | .50 | 1.49 | 17.80 | 2.57 | 11.00 | .090 | – | – | – | 2.00 | 1.77 | 3.90 | 4.78 |
| | .018 | .48 | 1.35 | 17.60 | 2.54 | 11.10 | .160 | – | – | – | 2.00 | 1.08 | 0.80 | 0.08 |

Table 10. Continued.

| Ref. | Composition [wt%] | | | | | | | | | | CRT [°C s ⁻¹] | Ferrite [pct] | | |
|-------|-------------------|------|------|-------|------|-------|------|------|-----|----|---------------------------|---------------|----------|----------|
| | C | Si | Mn | Cr | Mo | Ni | N | Cu | Nb | Ti | | Calc. | Exp. | Pred. |
| [133] | .015 | .55 | 1.46 | 17.60 | 2.31 | 11.10 | .220 | – | – | – | 2.00 | 0.33 | – | – |
| | .027 | .50 | 1.04 | 18.20 | .30 | 10.30 | .040 | .30 | – | – | .20 | 0.90 | 4.10 | 2.24 |
| | .045 | .40 | 1.60 | 18.25 | .30 | 9.05 | .030 | .30 | – | – | .20 | 4.06 | 5.72 | 3.81 |
| | .042 | .45 | 1.60 | 18.20 | .30 | 8.05 | .045 | .30 | – | – | .20 | 5.27 | 7.53 | 5.60 |
| | .042 | .40 | 1.31 | 18.39 | .36 | 12.59 | .015 | .27 | – | – | .20 | 0.51 | – | – |
| | .023 | .58 | 1.57 | 18.82 | .68 | 8.55 | .169 | .17 | – | – | .20 | 1.13 | 1.97 | 1.53 |
| [134] | .015 | .12 | 1.58 | 20.62 | 4.36 | 24.05 | .139 | 1.30 | – | – | .20 | – | – | – |
| | .024 | .49 | 1.23 | 18.18 | .45 | 8.58 | .047 | .16 | – | – | .20 | 5.08 | 8.20 | 6.85 |
| | .080 | 3.81 | 7.00 | 18.00 | – | 8.00 | .162 | – | – | – | .20 | 6.07 | 9.55 | 1.04 |
| | .040 | 3.74 | 8.60 | 18.00 | – | 8.00 | .160 | – | – | – | .20 | 6.23 | 5.32 | 1.80 |
| | .050 | 3.50 | 7.90 | 16.90 | – | 8.60 | .120 | – | – | – | .20 | 2.37 | 2.60 | – |
| | .050 | 3.80 | 8.90 | 17.00 | – | 9.00 | .161 | – | – | – | .20 | 1.55 | 0.15 | – |
| [135] | .050 | 3.70 | 7.90 | 17.70 | – | 8.60 | .178 | – | – | – | .20 | 2.60 | 0.25 | – |
| | .050 | 3.90 | 9.90 | 16.00 | – | 8.70 | .179 | – | – | – | .20 | 1.45 | 0.31 | – |
| | .056 | .39 | .83 | 18.10 | .10 | 8.10 | .049 | .20 | – | – | 36.00 | 4.52 | 5.50 | 4.23 |
| | .220 | 1.05 | 1.05 | 17.40 | 2.34 | 11.40 | .064 | .13 | .69 | – | 2.70 | 1.49 | – | – |
| | .210 | 1.06 | .89 | 17.40 | 2.05 | 11.00 | .062 | .11 | .57 | – | 2.70 | 1.47 | – | – |
| | .230 | 1.02 | 1.01 | 18.00 | 2.17 | 10.90 | .058 | .13 | .53 | – | 2.70 | 1.64 | – | – |
| [136] | .043 | .78 | 1.09 | 18.40 | .32 | 9.37 | .058 | .17 | – | – | 2.70 | 3.39 | 4.20 | 4.19 |
| | .038 | .40 | .56 | 17.90 | .11 | 10.70 | .027 | .05 | – | – | 2.70 | 0.48 | 1.80 | 0.18 |
| | .085 | .80 | .68 | 18.70 | .31 | 9.25 | .073 | .12 | – | – | 2.70 | 2.35 | 1.50 | 1.80 |
| | .076 | .87 | .93 | 18.90 | .23 | 9.19 | .062 | .12 | – | – | 2.70 | 3.56 | 2.80 | 3.56 |
| | .040 | 1.26 | .46 | 20.50 | .12 | 10.00 | .034 | .04 | – | – | 2.70 | 8.77 | 10.60 | 10.96 |
| | .033 | 1.34 | .42 | 19.50 | .12 | 10.00 | .037 | .04 | – | – | 2.70 | 6.60 | 6.50 | 9.31 |
| | .080 | .90 | .85 | 18.20 | .26 | 9.08 | .066 | .10 | – | – | 2.70 | 2.39 | 1.80 | 1.77 |
| | .038 | 1.10 | 1.00 | 17.70 | 2.20 | 9.62 | .048 | .14 | – | – | 2.70 | 8.28 | 8.10 | 9.83 |
| | .074 | 1.14 | .91 | 18.70 | 2.15 | 10.20 | .057 | .14 | .61 | – | 2.70 | 8.64 | 7.10 | 8.75 |
| | .070 | .94 | .97 | 18.70 | 2.23 | 11.10 | .057 | .14 | .72 | – | 2.70 | 5.34 | 3.60 | 7.02 |
| | .065 | .99 | .71 | 18.50 | 2.19 | 10.50 | .062 | .14 | .49 | – | 2.70 | 5.96 | 6.20 | 7.73 |
| | .036 | 1.15 | 1.08 | 17.70 | 2.18 | 10.10 | .034 | .18 | – | – | 2.70 | 8.34 | 8.10 | 9.59 |
| | .220 | 1.05 | 1.05 | 17.40 | 2.34 | 11.40 | .064 | .13 | .69 | – | .80 | 1.26 | – | – |
| | .210 | 1.06 | .89 | 17.40 | 2.05 | 11.00 | .062 | .11 | .57 | – | .80 | 1.25 | – | – |
| | .230 | 1.02 | 1.01 | 18.00 | 2.17 | 10.90 | .058 | .13 | .53 | – | .80 | 1.43 | – | – |
| | .043 | .78 | 1.09 | 18.40 | .32 | 9.37 | .058 | .17 | – | – | .80 | 3.11 | 4.60 | 4.19 |
| | .038 | .40 | .56 | 17.90 | .11 | 10.70 | .027 | .05 | – | – | .80 | 0.45 | 1.50 | 0.18 |
| | .085 | .80 | .68 | 18.70 | .31 | 9.25 | .073 | .12 | – | – | .80 | 2.01 | 2.40 | 1.80 |
| | .076 | .87 | .93 | 18.90 | .23 | 9.19 | .062 | .12 | – | – | .80 | 3.27 | 3.10 | 3.56 |
| | .040 | 1.26 | .46 | 20.50 | .12 | 10.00 | .034 | .04 | – | – | .80 | 8.48 | 11.30 | 10.96 |
| | .033 | 1.34 | .42 | 19.50 | .12 | 10.00 | .037 | .04 | – | – | .80 | 6.57 | 7.80 | 9.31 |
| | .080 | .90 | .85 | 18.20 | .26 | 9.08 | .066 | .10 | – | – | .80 | 2.08 | 1.70 | 1.77 |
| | .038 | 1.10 | 1.00 | 17.70 | 2.20 | 9.62 | .048 | .14 | – | – | .80 | 8.13 | 10.10 | 9.83 |
| | .074 | 1.14 | .91 | 18.70 | 2.15 | 10.20 | .057 | .14 | .61 | – | .80 | 8.52 | 8.30 | 8.75 |
| | .070 | .94 | .97 | 18.70 | 2.23 | 11.10 | .057 | .14 | .72 | – | .80 | 4.87 | 5.30 | 7.02 |
| | .065 | .99 | .71 | 18.50 | 2.19 | 10.50 | .062 | .14 | .49 | – | .80 | 5.55 | 6.50 | 7.73 |
| | .036 | 1.15 | 1.08 | 17.70 | 2.18 | 10.10 | .034 | .18 | – | – | .80 | 8.19 | 9.60 | 9.59 |
| | | | | | | | | | | | | Aver. Dev. | 1.12 pct | 2.40 pct |

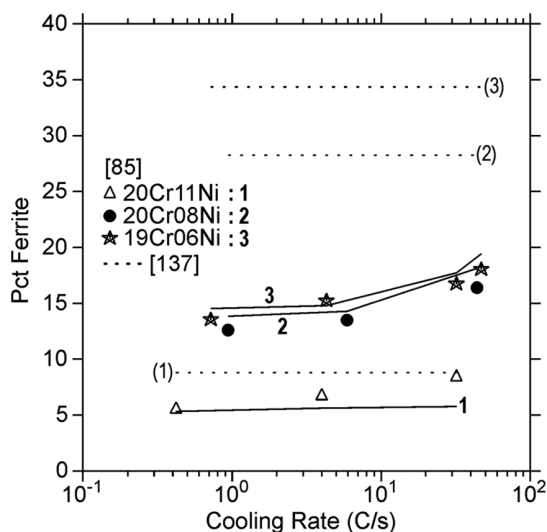


Figure 14. Calculated residual ferrite amounts in AISI 304 stainless steels as a function of cooling rate, together with experimental data points of Pereira^[85] and predictions by Schoefer^[137] (broken lines). The compositions of the steels are given in Table 10.

the possible pinning effect due to the formation of certain compounds (precipitates) resisting the growth is included. In the case of the secondary arm spacing, that effect comes from the compositions of Nb, Ti, and C (forming NbC and TiC), and in the case of the austenite grain size, the effect comes from the calculated fractions of all possible precipitates. In the latter case, it was not possible to characterize the pinning effects of different precipitate types, due to the lack of proper measurements for individual precipitates. According to Bernhard et al.^[10] and Schwerdtfeger et al.^[164], the pinning effect is

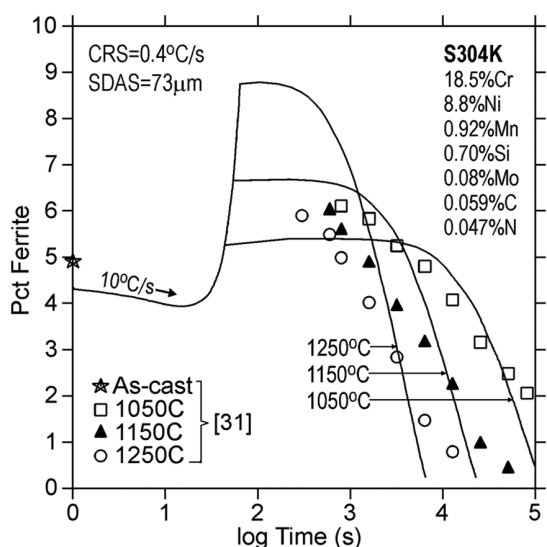


Figure 15. Calculated residual ferrite amounts in AISI 304 stainless steel (S304K) undergoing three different post-treatments, together with experimental data points of Kinoshita et al.^[31]

described with a specific ratio of the precipitate fraction and the radius, but missing detailed radius measurements for different types of precipitates, only the precipitate fraction dependency is considered in the SOL simulation. The austenite grain growth is resisted by the presence of ferrite, too, if present in steel. In that case, the pinning effect also includes the calculated ferrite fraction.

4.9. Miscellaneous Solidification Data

Finally, some miscellaneous DTA measurements from the study by Jernkontoret^[22] were compared with the SOL calculations. The calculations were done considering a cooling rate of 0.5 °C s^{-1} by applying the corresponding measured SDAS values.^[22] The observed and calculated formation temperatures of MnS (steel 209), NbC (steel 406), M_{23}C_6 (steel 414), and Ti compound (Ti_2CS , steel 415) were 1460 and 1455 °C (steel 209), 1330 and 1322 °C (steel 406), 1285 and 1279 °C (steel 414), and 1350–1305 and 1342 °C (steel 415), respectively. On the other hand, there are also some other thermal arrests in the study by Jernkontoret^[22], which could not be modeled by SOL.

5. Conclusion

IDS is a thermodynamic-kinetic software combining the microstructure tool developed over decades since 1984 to simulate the non-EQS of steels. The present work focused on describing the most essential features of its main calculation module, SOL, and the results that can be obtained with it. The proper mathematics or the specific applications of the module were not introduced in this study.

As the SOL module takes into account the kinetics of solidification depending on the time available for solute diffusion in dendrite arms, its simulation results lie somewhere between those obtained with purely thermodynamic software (assuming a full equilibrium between all phases) and with the modified Scheil model (assuming no solute diffusion for the slowly diffusing substitutional solutes in solid). Both calculation modes can be applied in SOL, by abbreviating the former calculations by EQS and the latter by PKS. Strictly speaking, the PKS calculations allow very low diffusivity for the substitutional solutes in solid to assure a successful simulation. By comparing the non-EQS calculations of SOL with those of EQS and PKS, it was found that in multicomponent steels, the solidus predicted by EQS calculations remains too high and drops too low by PKS calculations, regarding the nonequilibrium calculations and measurements. Also, the calculated amounts of precipitates become odd, as the EQS calculations predict far too high values and the PKS calculations give far too high temperatures for their formation. Nevertheless, both calculation modes can still give reasonable results for some low-alloyed steels, if applied for their solidification only.

Next, several simulations were made for a set of steels to introduce some interesting results of the SOL calculations, from a phenomenological point of view. The phenomena extensively studied in the literature are the formation and disappearance of ferrite and precipitates after solidification and during the subsequent post-treatments. The simulations revealed that by

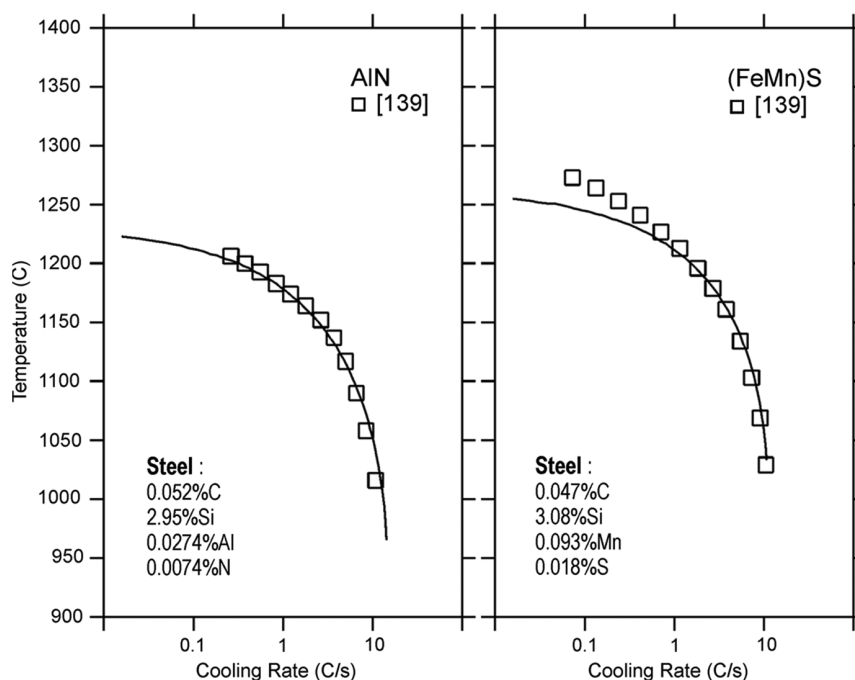


Figure 16. Calculated CCP curve of AlN and (Fe,Mn)S precipitation from ferrite, together with experimental data points of Iwayama and Haratani.^[139]

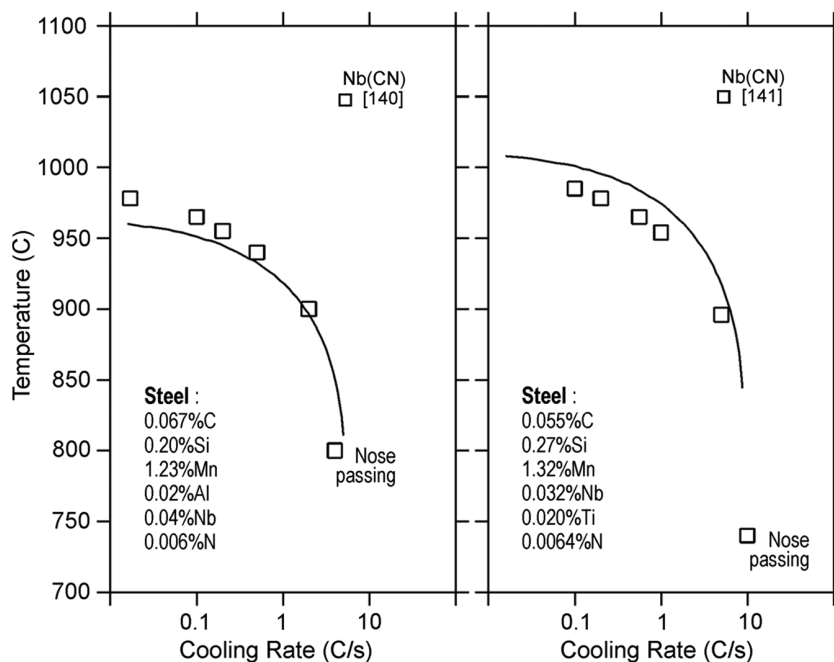


Figure 17. Calculated CCP curves of Nb(C,N) precipitation from austenite, together with experimental data points of Park et al.^[140] and Maehara et al.^[141]

a proper post-treatment, the residual ferrite amount in stainless steels can be controlled, for example, by making the undesired ferrite fraction dissolve from the final structure. The calculated residual ferrite amounts were later compared with numerous measurements showing that the SOL calculations compared quite well with the presence of residual ferrite in austenitic stainless steels, down to low temperatures, whereas on the basis of

equilibrium calculations, that ferrite tends to disappear at relatively high temperatures. Concerning the simulations made for the formation of precipitates and their dissolution, it was realized that one must design the post-treatment very carefully, to avoid unfavourable results. Several example simulations made for the precipitation of carbide NbC and carbonitride Nb(C,N) revealed that the desired presence of NbC in tool steel

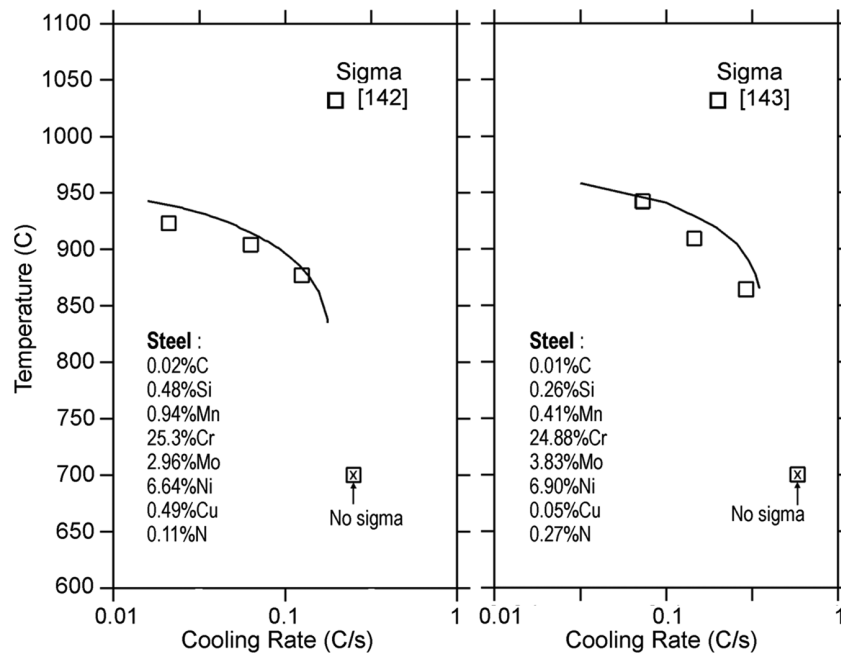


Figure 18. Calculated CCP curve of sigma phase precipitation from ferrite, together with experimental data points of Wilson and Nilsson^[142] and Stradomski and Dyja.^[143]

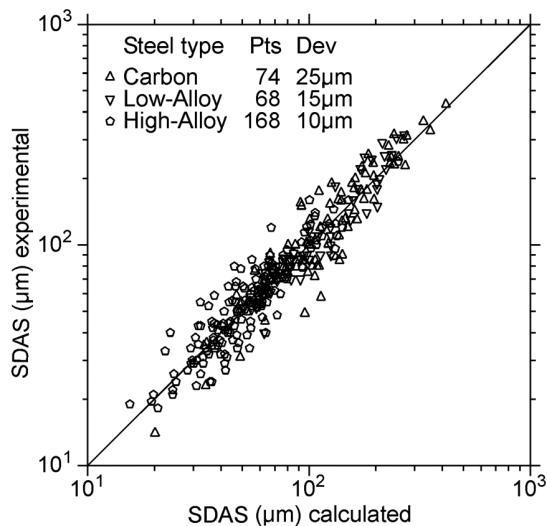


Figure 19. Calculated versus experimental^[22,26,45,85,87,90,98,148–160] SDAS in carbon, low-alloyed, and high-alloyed steels.

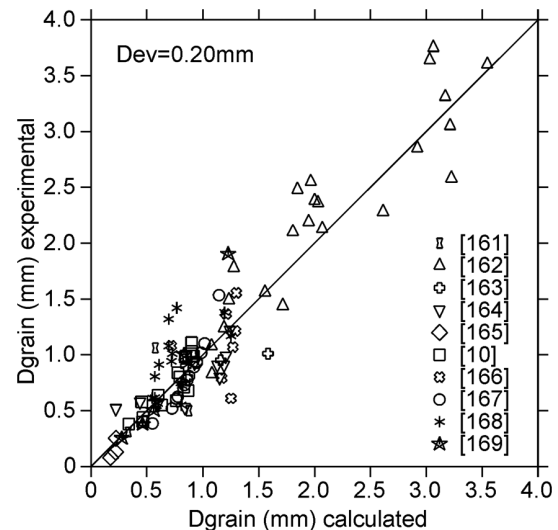


Figure 20. Calculated versus experimental^[10,161–169] austenite grain sizes in low-alloyed steels.

applications can be ensured by long-lasting post-treatments at reasonably low temperatures, whereas the formation of undesirable Nb(C,N) precipitates that can cause detrimental fine networks along the grain boundaries can be prevented by post-treatments made at a sufficiently high temperature, depending on the steel composition. Also demonstrated was the effect of alloying on the final amounts of Nb(C,N). As expected, by decreasing the C or Nb compositions of the example steel, the amounts of Nb(C,N) could be decreased. Similar results were also obtained in the case of Ti alloying, as the carbonitride

Ti(C,N) forming already from the liquid state ties up most of the N from the solution.

Finally, the SOL module calculations were validated with numerous solidification measurements of the literature, such as those for liquidus and solidus temperatures of different steels and the residual ferrite amounts in stainless steels. Also considered were the austenite formation temperatures (after the appearance of ferrite), the zero-strength temperatures, the solute microsegregations and partitions, the SDAS, and the austenite grain sizes. The agreement was good or reasonable

indicating an appropriate general validity of IDS simulations for different types of steels. This is a great advantage in comparison with the so-called “spearhead” models, which typically give good agreements only for some specific group of steels.

Acknowledgements

The research was conducted within the framework of the Genome of Steel project funded by the Academy of Finland (project #311934).

Conflict of Interest

The authors declare no conflict of interest.

Data Availability Statement

The data that support the findings of this study are available from the corresponding author upon reasonable request.

Keywords

microstructures, modeling, solidification, steels, thermodynamics

Received: February 17, 2022

Revised: May 12, 2022

Published online: May 29, 2022

- [1] H. Hu, S. A. Argyropoulos, *Modell. Simul. Mater. Sci. Eng.* **1996**, 4, 371.
- [2] B. G. Thomas, *Steel Res. Int.* **2017**, 89, 1700312.
- [3] M. Miltzer, *ISIJ Int.* **2007**, 47, 1.
- [4] J. Miettinen, Report TKK-MK-78, Helsinki University of Technology Publications in Materials Science and Metallurgy, Espoo, Finland **1999**.
- [5] J. Miettinen, S. Louhenkilpi, H. Kytönen, J. Laine, *Math. Comput. Simul.* **2010**, 80, 1536.
- [6] J. Miettinen, Project Report, University of Oulu, Oulu, Finland **2019**.
- [7] J. Miettinen, S. Louhenkilpi, V.-V. Visuri, T. Fabritius, *IOP Conf. Ser.: Mater. Sci. Eng.* **2019**, 529, 012063.
- [8] S. Louhenkilpi, J. Miettinen, J. Laine, R. Vesanen, I. Rentola, J. Moilanen, V.-V. Visuri, E.-P. Heikkinen, A. Jokilaakso, *IOP Conf. Ser.: Mater. Sci. Eng.* **2019**, 529, 012051.
- [9] T. Koseki, T. Matsumiya, W. Yamada, T. Ogawa, *Metall. Trans. A* **1994**, 25, 1309.
- [10] C. Bernhard, J. Reiter, H. Presslinger, *Metall. Mater. Trans. B* **2008**, 39, 885.
- [11] Y. Ueshima, S. Mizoguchi, T. Matsumiya, H. Kajioka, *Metall. Trans. B* **1986**, 17, 845.
- [12] M. Hillert, M. Jarl, *CALPHAD* **1978**, 2, 227.
- [13] B. Sundman, J. Ågren, *J. Phys. Chem. Solids* **1981**, 42, 297.
- [14] J. Miettinen, V.-V. Visuri, T. Fabritius, *Acta Univ. Oul. C* **2019**, 66, 704.
- [15] J. Miettinen, V.-V. Visuri, T. Fabritius, *Acta Univ. Oul. C* **2020**, 66, 758.
- [16] J. Miettinen, V.-V. Visuri, T. Fabritius, *Acta Univ. Oul. C* **2021**, 66, 787.
- [17] E. Scheil, *Z. Metallkd.* **1942**, 34, 70.
- [18] Q. Chen, B. Sundman, *Mater. Trans. JIM* **2002**, 43, 551.
- [19] J.-O. Andersson, T. Helander, L. Höglund, P. Shi, B. Sundman, *CALPHAD* **2002**, 26, 273.
- [20] T. W. Clyne, W. Kurz, *Metall. Trans. A* **1981**, 12, 965.
- [21] A. Borgenstam, A. Engström, L. Höglund, J. Ågren, *J. Phase Equilib.* **2000**, 21, 269.
- [22] Jernkontoret, *A Guide to the Solidification of Steels*, Jernkontoret, Stockholm, Sweden, **1977**.
- [23] N. Suutala, T. Takalo, *Metall. Trans. A* **1979**, 10, 512.
- [24] S. David, *Weld Res. Suppl.* **1981**, 63.
- [25] Y. Y. Lee, S. K. Kim, *J. Korean Inst. Met. Mater.* **1992**, 30, 1104.
- [26] M. Wolf, *Ironmaking Steelmaking* **1986**, 13, 258.
- [27] A. Astaf'ev, L. Lepekhina, N. Batieva, *Met. Sci. Heat Treat.* **1989**, 31, 880.
- [28] H. C. Campbell, *Welding J.* **1975**, 54, 867.
- [29] G. Brouwer, *Philips Weld. Rep.* **1978**, 3, 16.
- [30] S. H. Kim, H. K. Moon, T. Kang, C. S. Lee, *Mater. Sci. Eng.* **2003**, A356, 390.
- [31] Y. Kinoshita, S. Takeda, H. Yoshimura, *Tetsu to Hagane* **1979**, 65, 1176.
- [32] S. Raghunathan, V. Seetharaman, S. Venkadesan, P. Rodriguez, *Metall. Mater. Trans. A* **1979**, 10, 1683.
- [33] NiobelCon—Consulting services for the metallurgy of industry, Schilde, Belgium, <https://www.niobelcon.com/NiobelCon/niobium/>
- [34] M. Vedani, D. Ripamonti, A. Mannucci, D. Dellasega, *La Metall. Ital.* **2008**, 100, 19.
- [35] D. N. Crowther, in *Proc. Vanitec Symp.*, Beijing, China, **2001**, p. 99.
- [36] J. Miettinen, Project Report, Casim Consulting Oy, Espoo, Finland **2009**.
- [37] K. Löhberg, W. Schmidt, *Arch. Eisenhüttenwes.* **1938**, 11, 607.
- [38] E. Schürmann, J. von Schweinichen, *Giessereiforschung* **1986**, 38, 125.
- [39] C. Bernhard, R. Pierer, P. Presoly, S. Griesser, P. Krajewski, *COMET Workshop*, Leoben, Austria, **2011**.
- [40] A. J. W. Ogilvy, A. Ostrowski, D. H. Kirkwood, *Met. Sci.* **1981**, 15, 168.
- [41] D. M. Kundrat, M. Chochol, J. F. Elliott, *Metall. Trans. B* **1984**, 15, 663.
- [42] W. R. Thorpe, B. Chicco, *Metall. Trans. A* **1985**, 16, 1541.
- [43] E. Schürmann, H. Fischer, T. Degen, *Giessereiforschung* **1991**, 43, 91.
- [44] S.-E. Amara, A. Belhadj, R. Kesri, S. Hamar-Thibault, Z. Metallkd, **1999**, 90, 116.
- [45] H. Jacobi, K. Wünnenberg, *Steel Res.* **1999**, 70, 362.
- [46] E. Schürmann, I. K. Geissler, *Giessereiforschung* **1977**, 29, 153.
- [47] T. Takei, *Kinzoku no Kenkyu* **1932**, 9, 97.
- [48] R. A. Buckley, W. Hume-Rothery, *J. Iron Steel Inst.* **1964**, 202, 895.
- [49] T. Kase, *Sci. Rep. Tohoku Imp. Univ., Ser. 1* **1925**, 14, 193.
- [50] J. E. Hilliard, W. S. Owen, *J. Iron Steel Inst.* **1952**, 172, 268.
- [51] W. Patterson, G. Hülsenbeck, H. A. S. Madi, *Giessereiforschung* **1968**, 20, 49.
- [52] P. Presoly, R. Pierer, C. Bernhard, *Metall. Mater. Trans. A* **2013**, 44, 5377.
- [53] P. Presoly, Private Communication, Department of Metallurgy, Montanuniversität Leoben, Leoben, Austria, **2014**.
- [54] M. Oya, *Sci. Rep. Tohoku Univ.* **1930**, 19, 449.
- [55] I. I. Kornilov, Iron alloys, Vol. 1, Alloys of iron–chromium–aluminium, Izdatel'stvo Akad. Nauk SSSR, Moscow/Leningrad, Soviet Union, **1945**.
- [56] V. A. Kozheurov, M. A. Ryss, S. E. Pigasov, V. I. Antonenko, Y. S. Kuznetsov, G. G. Mikhailov, I. Y. Pashkeev, *Sb. Chelyab. Elektromet. Kombinata* **1970**, 69.
- [57] K. Moriwaki, *Tetsu to Hagane* **1939**, 25, 396.
- [58] D. M. Kundrat, J. F. Elliott, *Metall. Trans. A* **1986**, 17, 1461.
- [59] D. M. Kundrat, J. F. Elliott, *Metall. Trans. A* **1986**, 17, 1825.
- [60] J. W. Putman, R. D. Potter, M. J. Grant, *Trans. ASM* **1951**, 43, 824.
- [61] S. Takeda, N. Yukawa, *J. Jpn. Inst. Met.* **1957**, 21, 275.
- [62] M. Choccol, Doctoral Thesis, Massachusetts Institute of Technology, Cambridge, MA, USA, **1976**.
- [63] E. Schürmann, J. Brauckmann, *Arch. Eisenhüttenwes.* **1977**, 48, 3.
- [64] D. M. Kundrat, J. F. Elliott, *Metall. Trans. A* **1988**, 19, 899.

- [65] E. Schürmann, M. Durdevic, T. Degen, *Steel Res.* **1994**, 65, 517.
- [66] W. Z. Denecke, *Anorg. Chem.* **1926**, 154, 178.
- [67] R. Vogel, B. Wenderott, *Arch. Eisenhüttenwes.* **1940**, 14, 279.
- [68] V. W. Köster, W. Dannöhl, *Z. Metallkunde* **1935**, 27, 220.
- [69] I. Gallino, S. Curiotto, M. Baricco, M. E. Kassner, R. Busch, *J. Phase Equilib. Diff.* **2008**, 29, 131.
- [70] E. Schürmann, M. Djurdjevic, L. Nedeljkovic, *Steel Res.* **1997**, 68, 383.
- [71] R. Vogel, H.-J. Wallbaum, *Arch. Eisenhüttenwes.* **1938**, 12, 299.
- [72] W. Köster, W. Tonn, *Arch. Eisenhüttenwes.* **1933**, 7, 356.
- [73] N. Parravano, *Int. Z. Metallorg.* **1913**, 4, 171.
- [74] R. Vogel, H. Bedarff, *Eisenhüttenwes.* **1937**, 10, 581.
- [75] W. Dannöhl, *Wiss. Veröff. Siemens Werke* **1938**, 17, 1.
- [76] R. Vogel, R. Gerhardt, *Arch. Eisenhüttenwes.* **1961**, 32, 47.
- [77] H. P. Takeda, K. Mutuzaki, *Tetsu to Hagane* **1940**, 26, 335.
- [78] M. C. J. Marker, B. Skolyszewska-Kühberger, H. S. Effenberger, C. Schmetterer, K. W. Richter, *Intermetallics* **2011**, 19, 1919.
- [79] A. Yutaka, *J. Jpn. Inst. Met.* **1941**, 5, 136.
- [80] F. Wever, W. Jellinghaus, *Mitt. Kaiser-Wilhelm-Inst. Eisenforsch.* **1931**, 13, 93.
- [81] W. F. Roeser, T. Wensel, Research paper RP1375, National Bureau of Standards, Vol. 26, **1941**.
- [82] C.-Å. Däcker, H. Fredriksson, STU Rapport, Institution för Metallernas Gjutting, KTH Royal Institute of Technology, Stockholm, Sweden **1976**.
- [83] L. Erickson, *Scand. J. Metall.* **1977**, 6, 116.
- [84] B. Leffler, S. Malm, *Metals Technology* **1977**, 9, 81.
- [85] O. Pereira, Doctoral Thesis, University of Sheffield, Sheffield, United Kingdom, **1979**.
- [86] B. Callmer, O. Grimmer, *Scand. J. Metall.* **1980**, 9, 151.
- [87] N. Suutala, Licentiate Thesis, University of Oulu, Oulu, Finland, **1980**.
- [88] M. Bobadilla, G. Lesoult, *Mem. Etud. Sci. Rev. Met.* **1981**, 78, 345.
- [89] P. Hooli, Private Communication, Outokumpu Oy, Tornio, Finland, **1982**.
- [90] M. A. Taha, H. Jacobi, M. Imagumbai, K. Schwerdtfeger, *Metall Trans. A* **1982**, 13, 2131.
- [91] J. Loh, Doctoral Thesis, Rheinisch-Westfälische Technische Hochschule Aachen, Aachen, Germany, **1984**.
- [92] S. Kobayashi, *Trans. ISIJ* **1988**, 28, 535.
- [93] P. Kangas, Internal Report of Outokumpu Polarit, Tornio, Finland **1989**.
- [94] A. A. Howe, ECSC Research Project Report EUR13302, The European Commission, **1991**.
- [95] R. Arola, VTT Research Notes 1732, Manufacturing Technology, VTT, Espoo, Finland, **1996**.
- [96] P. Hooli, Outokumpu Polarit internal report, **1996**.
- [97] G. Allan, ECSC Research project, Report EUR13941, The European Commission, **1997**.
- [98] B. Weisgerber, M. Hecht, K. Harste, *Steel Res.* **1999**, 70, 403.
- [99] D. J. Seol, Y. M. Won, K. H. Oh, Y. C. Shin, C. H. Yim, *Iron Steel Inst. Jpn.* **2000**, 40, 356.
- [100] A. F. Padilha, I. F. Machado, R. L. Plaut, *J. Mater. Proc. Technol.* **2005**, 170, 89.
- [101] R. A. Howell, Doctoral Thesis, Missouri University of Science and Technology, Rolla, Missouri, USA, **2009**.
- [102] K. D. Carlsson, C. Beckermann, *Int. J. Cast Metall. Res.* **2012**, 25, 75.
- [103] A. Ferraiuolo, A. Smith, J. G. Sevillano, F. de las Cuevas, P. Karjalainen, G. Pratolongo, H. Gouveia, M. M. Rodrigues, Contract No RFSR-CT-2005-00030, Publications Office of the European Union, Luxembourg, **2012**.
- [104] K. Gryc, B. Smetana, M. Tkadleckova, M. Žaludova, K. Michalek, L. Socha, J. Dobrovska, K. Janiszewski, P. Machovcak, *Metallurgija* **2014**, 53, 295.
- [105] G. Klančnik, J. Medved, A. Nagode, *J. Therm. Anal. Calorim.* **2014**, 116, 295.
- [106] Z. Han, J. Liu, Y. He, K. Li, Y. Ji, J. Liu, *Int. J. Miner. Metall. Mater.* **2015**, 22, 1141.
- [107] C.-L. Zhuang, J.-H. Liu, C. Bernhard, P. Presoly, *J. Iron Steel Res. Int.* **2015**, 22, 709.
- [108] G. Klančnik, D. Steiner Petrovič, J. Medved, *J. Miner. Metall. Sect. B* **2012**, 48, 383.
- [109] O. Martinik, B. Smetaná, J. Dobrovská, S. Zlá, M. Kawulková, K. Gryc, P. Dostál, L. Drozdová, B. Bauditšová, *J. Miner. Metall. Sect. B* **2017**, 53, 391.
- [110] O. Martinik, B. Smetaná, J. Dobrovská, S. Zlá, M. Kawulková, K. Gryc, L. Drozdová, P. Dostál, B. Martiníková, *J. Phase Equilib. Diff.* **2019**, 40, 93.
- [111] R. B. Tuttle, *Arch. Foundry Eng.* **2019**, 19, 83.
- [112] R. H. A. Abas, *Eng. Tech. J.* **2013**, 31, 432.
- [113] E. Kivineva, N. Suutala, Report 5397-109/87, Outokumpu Oy, Tornio, Finland **1987**.
- [114] E. Schürmann, T. Stišović, *Stahl Eisen* **1998**, 118, 97.
- [115] Z. Han, K. Cai, B. Liu, *ISIJ Int.* **2001**, 41, 1473.
- [116] J. Štětina, Doctoral Thesis, Technical University of Ostrava, Ostrava, Czech Republic, **2007**.
- [117] J. Sivula, Report VTT-MRG B-8603, Technical Research Centre of Finland, Espoo, Finland **1986**.
- [118] K. C. Mills, *Recommended Values of Thermophysical Properties for Selected Commercial Alloys*, ASM International, Woodhead Publishing Ltd., Cambridge, MA, USA **2002**.
- [119] F. Binczyk, *Arch. Foundry Eng.* **2007**, 7, 21.
- [120] H. Kawashima, K. Sigeno, M. Kusubae, K. Tachibana, *Mater. Trans.* **2011**, 52, 2184.
- [121] R. Lora, A. Dioszegi, L. Elmquist, *Key Eng. Mater.* **2011**, 457, 108.
- [122] E. Moumeni, J. H. Hattel, N. S. Tiedje, A. Horwell, *Solidification of Cast Iron – A Study on the Effect of Microalloy Elements on Cast Iron*, Technical University of Denmark, Kongens Lyngby, Denmark **2013**.
- [123] G. Alonso, X. Durango, S. M. Stefanescu, R. Suarez, A. Loizaga, G. Zarrabeitia, *Int. Foundry Res.* **2014**, 66, 1.
- [124] K. Janerka, M. Kondracki, J. Jezierski, J. Szajnar, M. Stawarz, *J. Mater. Eng. Perform.* **2014**, 23, 2174.
- [125] V. E. A. dos Anjos, Doctoral Thesis, University of Duisburg-Essen, Essen, Germany, **2015**.
- [126] A. Natxiondo, R. Suarez, J. Sertucha, P. Larranaga, *Metals* **2015**, 5, 239.
- [127] Y. M. Won, K. H. Kim, T. Yeo, K. H. Oh, *Iron Steel Inst. Jpn* **1998**, 38, 1093.
- [128] G. Shin, T. Kajitani, T. Suzuki, T. Umeda, *Tetsu to Hagane* **1992**, 78, 587.
- [129] A. Yamanaka, K. Nakajima, K. Okamura, *Ironmaking Steelmaking* **1995**, 22, 508.
- [130] E. Schmidtman, K. Rakoski, *Arch. Eisenhüttenwes.* **1983**, 54, 357.
- [131] T. Nakagawa, T. Umeda, J. Murata, Y. Kamimura, N. Niwa, *ISIJ Int.* **1992**, 35, 723.
- [132] M. S. F. de Lima, *Mater. Res.* **2012**, 15, 32.
- [133] A. Spaccarotella, R. Fleisch, P. Scheller, CSM Report TR336, Centro Sviluppo Materiali, Roma **2000**.
- [134] A. Gigović-Gekić, M. Oruč, M. Gojić, in *Proc. 15th Int. Research/Expert Conference on Trends in the Development of Machinery and Associated Technology*, Prague, Czech Republic, **2011**, pp. 157–160.
- [135] S. Fukumoto, Y. Iwasaki, H. Motomuraans, Y. Fukuda, *ISIJ Int.* **2012**, 52, 74.

- [136] A. F. Padilha, C. F. Tavares, M. A. Martorano, *Mater. Sci. Forum* **2013**, 730–732, 733.
- [137] E. A. Schoefer, in *Metals Handbook*, Vol. 15, ASM International, Metals Park, Ohio, USA, **1988**, p. 725.
- [138] J. Glowina, B. Kalandyk, K. Hübner, *Mater. Charact.* **2001**, 47, 149.
- [139] K. Iwayama, T. Haratani, J. *Magn. Magn. Mater.* **1980**, 19, 15.
- [140] S. H. Park, S. Yue, J. J. Jonas, *Metall. Trans. A* **1979**, 23, 1641.
- [141] J. Chen, S. Tang, Z. Liu, G. Wang, Y. Zhou, *J. Mater. Sci.* **2012**, 47, 4640.
- [142] Y. Maehera, M. Koike, N. Fujino, T. Kunitake, *Trans. ISIJ* **1983**, 12, 240.
- [143] A. Wilson, J.-O. Nilsson, *Scand. J. Metall.* **1996**, 25, 178.
- [144] Z. Stradomski, D. Dyja, in *Proceedings of 4th Youth Symp. on Experimental Solid Mechanics*, Castrocaro Terme, Italy, **2005**.
- [145] A. Rose, H. Hougardy, *Atlas zur Wärmebehandlung der Stähle*, vol. 2, Verlag Stahleisen m.b.H., Düsseldorf, Germany, **1972**.
- [146] G. F. van der Voort, *Atlas of Time–Temperature Diagrams for Irons and Steels*, ASM International, Metals Park, OH, USA **1991**.
- [147] J. Miettinen, S. Koskenniska, M. Somani, S. Louhenkilpi, A. Pohjonen, J. Larkiola, J. Kömi, *Metall. Mater. Trans B* **2019**, 50, 2853.
- [148] A. Suzuki, T. Suzuki, Y. Nakaoga, Y. Iwata, *J. Jpn. Inst. Met.* **1968**, 32, 1301.
- [149] A. Suzuki, Y. Nakaoga, *J. Jpn. Inst. Met.* **1969**, 33, 658.
- [150] M. C. Flemings, D. R. Poirier, R. V. Barone, *J. Iron Steel Inst.* **1970**, 208, 371.
- [151] K. Schwerdtfeger, *Arch. Eisenhüttenwes.* **1970**, 41, 923.
- [152] H. Jacobi, K. Schwerdtfeger, *Metall. Trans. A* **1976**, 7, 811.
- [153] T. Okamoto, S. Matsuo, K. Kishitake, *Tetsu to Hagane* **1977**, 63, 936.
- [154] M. Wolf, Doctoral Thesis, École Polytechnique Fédérale de Lausanne, Lausanne, Switzerland, **1978**.
- [155] T. Okamoto, K. Kishitake, K. Murakami, *Trans. ISIJ* **1981**, 21, 641.
- [156] B. Rogberg, Report of R&D Centre, AB Sandvik Steel, Stockholm, **1984**.
- [157] M. Imagumbai, *ISIJ Int.* **1994**, 134, 574.
- [158] M. Imagumbai, *ISIJ Int.* **1994**, 134, 896.
- [159] A. E. Ares, R. Caram, C. T. Rios, C. E. Schvezov, *Matéria* **2003**, 8, 70.
- [160] M. Kudoh, B. Wo, *Steel Res.* **2003**, 74, 161.
- [161] Y. Maehara, K. Yasumoto, Y. Sugitani, K. Gunji, *Trans. ISIJ* **1985**, 25, 1045–1052.
- [162] K. Yasumoto, T. Nagamichi, Y. Maehara, K. Gunji, *Tetsu to Hagane* **1987**, 73, 1738.
- [163] B. Mintz, R. Abushosha, *Mater. Sci. Technol.* **1992**, 8, 171.
- [164] K. Schwerdtfeger, A. Köthe, J. M. Rodriguez, W. Bleck, *EUR 19409/1 EN*, Vol. 1, Luxembourg, **2001**, pp. 33–48.
- [165] K. Hirata, O. Umezawa, K. Nagai, *Mater. Trans.* **2002**, 43, 305.
- [166] Y. Kobayashi, S. Iwasaki, K. Nakazato, T. Hibar, S. Kuroda, N. Sakuma, N. Yoshida, K. Nagai, *ISIJ Int.* **2008**, 48, 344.
- [167] Y. Ohba, S. Kitade, I. Takasu, *ISIJ Int.* **2008**, 48, 350.
- [168] H. Ohta, R. Inoue, H. Suito, *ISIJ Int.* **2008**, 48, 294.
- [169] M. Sasaki, K. Matsuura, K. Ohsasa, M. Ohno, *ISIJ Int.* **2009**, 49, 1362.